ACS NANO

www.acsnano.org

ARTICLE

Modulation of Intratumoral *Fusobacterium nucleatum* to Enhance Sonodynamic Therapy for Colorectal Cancer with Reduced Phototoxic Skin Injury

Xiao Qu,[⊥] Fang Yin,[⊥] Manman Pei,[⊥] Qian Chen,* Yuanyuan Zhang, Shengwei Lu, Xuelian Zhang, Ziyuan Liu, Xinyao Li, Hangrong Chen, Yang Zhang,* and Huanlong Qin*

Cite This: *ACS Nano* 2023, 17, 11466–11480

Read Online

ACCESS | Metrics & More | Article Recommendations | Supporting Information

ABSTRACT: **Intratumoral pathogens can contribute to cancer progression and affect therapeutic response. *Fusobacterium nucleatum*, a core pathogen of colorectal cancer (CRC), is an important cause of low therapeutic efficacy and metastasis. Thus, the modulation of intratumoral pathogens may provide a target for cancer therapy and metastasis inhibition. Herein, we propose an intratumoral *F. nucleatum*-modulating strategy for enhancing the therapeutic efficacy of CRC and inhibiting lung metastasis by designing an antibacterial nanoplatform (Au@BSA-CuPpIX), which produced reactive oxygen species (ROS) under ultrasound and exhibited strong antibacterial activity. Importantly, Au@BSA-CuPpIX reduced the levels of apoptosis-inhibiting proteins by inhibiting intratumoral *F. nucleatum*, thereby enhancing ROS-induced apoptosis. *In vivo* results demonstrated that Au@BSA-CuPpIX effectively eliminated *F. nucleatum* to enhance the therapeutic efficacy of sonodynamic therapy (SDT) for orthotopic CRC and inhibit lung metastasis. Notably, entrapped gold nanoparticles reduced the phototoxicity of metalloporphyrin accumulated in the skin during tumor treatment, preventing severe inflammation and damage to the skin. Therefore, this study proposes a strategy for the elimination of *F. nucleatum* in CRC to enhance the therapeutic effect of SDT, thus providing a promising paradigm for improving cancer treatment with fewer toxic side effects and promoting the clinical translational potential of SDT.**

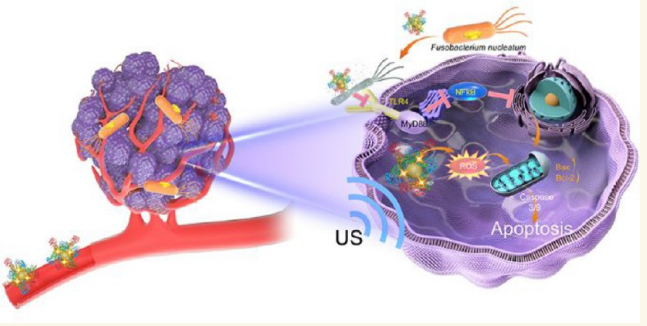

KEYWORDS: *Fusobacterium nucleatum, intratumoral bacteria, sonodynamic therapy, skin injury, colorectal cancer*

INTRODUCTION

The occurrence and development of colorectal cancer (CRC) are influenced by intratumoral pathogens which are significant environmental factors.[1−4] To date, multiple pathogenic strains have been reported to promote CRC progression and are considered potential therapeutic targets in clinical practice, such as enterotoxigenic *Bacteroides fragilis*, enteropathogenic *Escherichia coli*, and *Fusobacterium nucleatum*.[5,6] Although different CRC-associated pathogens (*e.g.*, *Peptostreptococcus Stomatis*) have been progressively identified in studies on patients with CRC, it has been confirmed by numerous studies that *F. nucleatum* is the main pathogen responsible for CRC.[7−9] CpG island methylation in tumor cells, microsatellite instability, and mutations in proto-oncogenes (BRAF and KRAS genes) are affected by an increased abundance of *F. nucleatum*, which is a Gram-negative anaerobic bacterium, in CRC tissues. Moreover, the presence of *F. nucleatum* reduces the number of CD3+ T cells in tumor tissues.[10−12] The pathogenic role of *F. nucleatum* in CRC has been extensively studied, and it has been found that *F. nucleatum* activates β-catenin signaling by binding to E-cadherin using its specific FadA adhesion protein, which subsequently enhances the expression of oncogenes and inflammatory genes.[13] By acting on inhibitory immune receptors of natural killer cells (NK cells), the Fap2 protein from *F. nucleatum* can trigger an

Received: February 10, 2023
Accepted: April 19, 2023
Published: May 18, 2023

https://doi.org/10.1021/acsnano.3c01308
ACS Nano 2023, 17, 11466−11480

Scheme 1. Scheme depicts the procedure for synthesizing Au@BSA-CuPpIX and the mechanism of eliminating the core pathogenic bacteria in CRC in order to boost the therapeutic effect of SDT together with reduced skin photosensitivity. (a) Schematic description of the Au@BSA-CuPpIX synthesizing process. (b) Au@BSA-CuPpIX reduces the level of apoptosis-inhibiting proteins by inhibiting *F. nucleatum* to advance the efficacy of SDT for orthotopic CRC with lung metastasis restriction. (c) Au@BSA-CuPpIX effectively reduces the phototoxicity of metalloporphyrin accumulated in the skin during tumor treatment, preventing severe inflammation and damage to the skin.

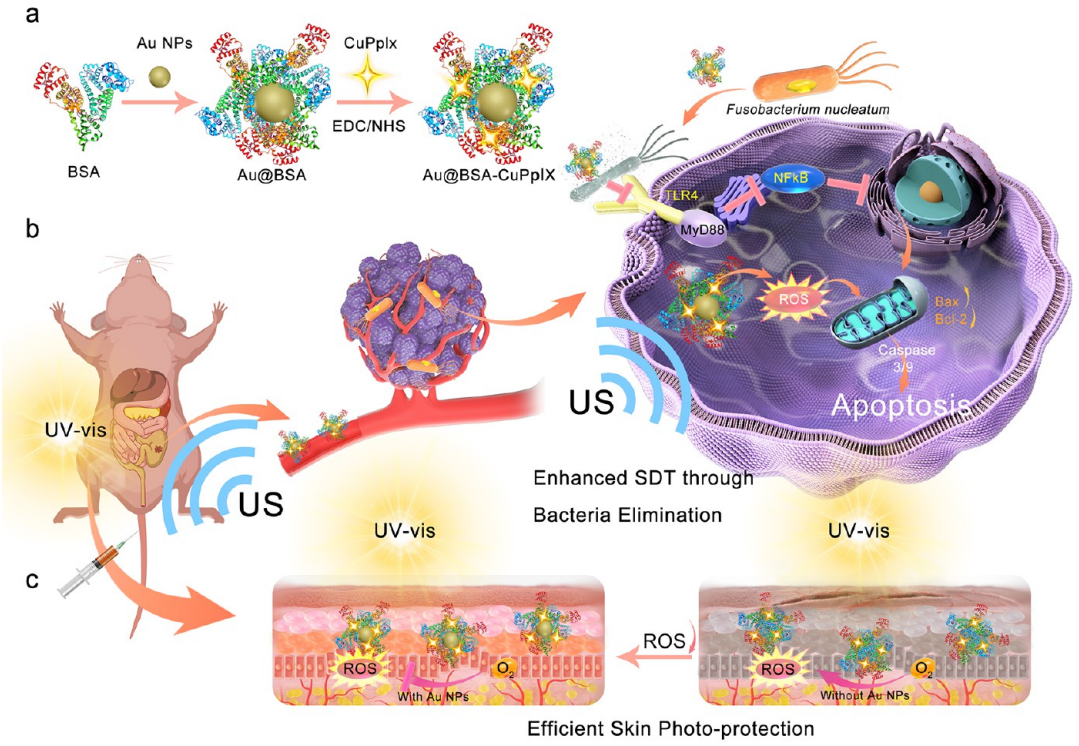

immune escape mechanism in tumor cells.[14,15] The recognition of *F. nucleatum*'s lipopolysaccharide by Toll-like receptor 4 (TLR4) on the cell surface is a critical mechanism that triggers the TLR4/MyD88 cascade to activate the nuclear factor-κB (NF-κB) pathway, ultimately leading to the up-regulation of cell proliferation and apoptosis inhibition genes.[16] Several reports have found that the abundance of intratumoral *F. nucleatum* is associated with poor prognosis in CRC and shares a high positive correlation with postoperative tumor recurrence, all of which indicate that *F. nucleatum* may reduce the effectiveness of CRC treatment through microbial metabolites or activation of apoptosis suppressor genes.[1,17−19] Prior research indicates that infection of *F. nucleatum* can trigger the TLR4/AKT/Keap1/NRF2 pathway, enhance the CYP2J2 expression in CRC cells, and ultimately lead to the increased production of 12,13-EpOME, which promotes the advancement of CRC.[20,21] *F. nucleatum* activates the TLR4/MyD88 autophagy pathway and boosts the mRNA expression levels of autophagy-related genes ULK1 and ATG7, elevating the autophagy level of CRC cells, resulting in resistance to 5-fluorouracil (5-Fu) and oxaliplatin (OxPt) and reducing chemotherapy-induced apoptosis.[18] As a result, the presence of *F. nucleatum* within CRC not only enhances the onset and progression of CRC but also impacts the therapeutic efficacy and cancer metastasis.

Due to its ability to deeply penetrate tissues and ensure safety, sonodynamic therapy (SDT) shows great potential as a supplementary technique to traditional cancer treatments, making it an emerging and promising method in the field of cancer treatment.[22−26] Ultrasonic (US) is utilized by SDT to stimulate sonosensitizers, resulting in the generation of reactive oxygen species (ROS) that trigger cancer cell apoptosis.[27−29] Currently, organic sonosensitizers for SDT are frequently developed from organic porphyrins and their derivatives, such as hematoporphyrin, protoporphyrin IX, and hematoporphyrin monomethyl ether,[23,30−34] because of their exceptional attributes including extensive π-electron-conjugated systems as well as versatile optoelectronic and catalytic features.[22,35] Several porphyrin-based sonosensitizers have been reported to show effective ROS production upon US radiation for tumor treatment.[36,37] However, the TLR4/NF-κB pathway in CRC cells is triggered by *F. nucleatum* infection, leading to the activation of various antiapoptosis target genes, including TNFR-associated factor (TRAF-1, TRAF-2),[38] BIRC3,[39] inhibitor of apoptosis proteins (IAPs),[40] and Bcl-2,[41−43] which resists ROS and promotes cell survival.[44] Therefore, integrating the elimination of intratumoral *F. nucleatum* and SDT is likely to provide the best choice for improving the efficacy of SDT and obtaining high clinical therapeutic value.

However, with the exception of tumor accumulation, some sonosensitizers accumulate in the skin and other superficial tissues for a long time. Considering that organic sonosensitizers are mostly derived from photosensitizers, they can be excited by sunlight and indoor light to produce ROS, which causes severe inflammation and damage after administration, posing a potential threat to SDT application in tumor therapy.[45−47] Therefore, it is crucial for SDT applications to alleviate the phototoxicity of sonosensitizers on normal skin. Recently, some nanoplatforms in the field of photodynamic therapy, including near-infrared light-activating DiR-hCe6-

https://doi.org/10.1021/acsnano.3c01308
ACS Nano 2023, 17, 11466−11480

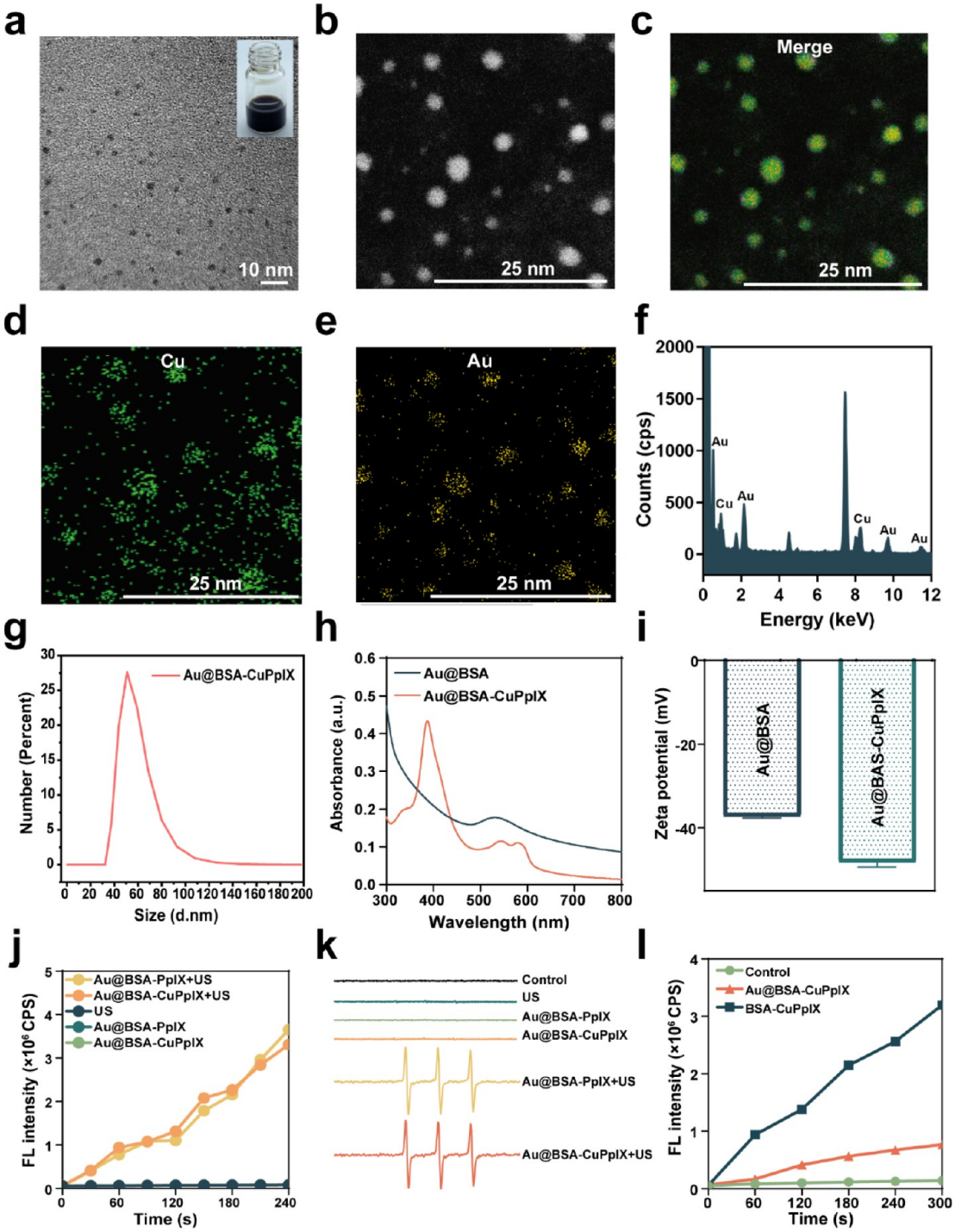

Figure 1. Characteristics of Au@BSA-CuPpIX. (a) TEM image of Au@BSA-CuPpIX. Insets in the upper right: digital photograph of Au@BSA-CuPpIX dissolved in deionized water. (b) HAADF image of Au@BSA-CuPpIX. (c–e) Elemental mapping of Au and Cu. (f) EDS analysis of Au@BSA-CuPpIX. (g) Size distribution of Au@BSA-CuPpIX. (h) UV–vis absorption spectra and (i) zeta potential of Au@BSA and Au@BSA-CuPpIX. (j) Fluorescence intensity of SOSG examined under different conditions with or without US radiation. (k) ESR spectra of control, US, Au@BSA-PpIX, Au@BSA-CuPpIX, Au@BSA-PpIX+US, and Au@BSA-CuPpIX+US groups; 2,2,6,6-tetramethylpiperidine as trapping agent. (l) Fluorescence intensity of SOSG under different conditions with light radiation (405 nm, 5 mW/cm^2).

liposome and biodegradable Ce6@$CaCO_3$-PDA, have been designed for tumor treatment with reduced skin phototoxicity.[48−50] Although these ingenious strategies show effective tumor therapy with skin protection, several limitations need to be addressed to apply these strategies for tumor SDT. Such responsive coencapsulated nanosystems could release photosensitizers or sonosensitizers in the blood circulation or tumor tissue, causing photodamage to the skin. Therefore, the design of an SDT nanosystem that is permanently silent to sunlight and indoor light is beneficial for promoting the clinical application of tumor SDT.

https://doi.org/10.1021/acsnano.3c01308
ACS Nano 2023, 17, 11466−11480

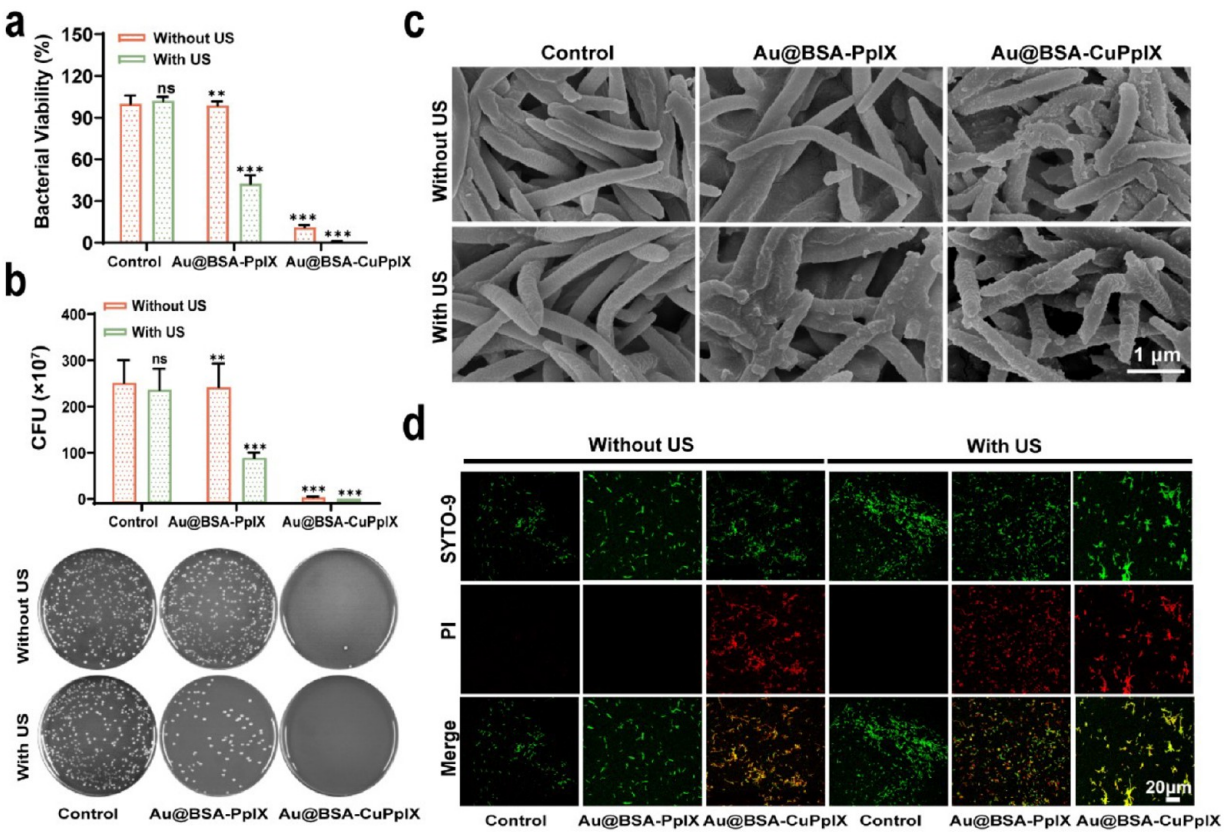

Figure 2. Antibacterial performance of Au@BSA-CuPpIX. (a) Statistical analysis of the bacterial activity of *F. nucleatum* treated with different groups. The concentrations of Au@BSA-CuPpIX and Au@BSA-PpIX were set at 100 μg mL^{-1} (n = 3). (b) The colony forming unit (CFUs) statistics of *F. nucleatum* after different treatments (n = 3) and plate photographs of *F. nucleatum* forming colony after different treatments. (c) SEM of *F. nucleatum* after different treatments. (d) After various treatments, live and dead *F. nucleatum* were subjected to confocal imaging using staining techniques.

Herein, an ultrasonic stimulation-responsive albumin-based nanoplatform (Au@BSA-CuPpIX) with antibacterial function was designed and synthesized employing bovine serum albumin (BSA) to be a carrier and stabilizer, which entraps Au nanoparticles (Au NPs) by biomimetic mineralization and is further modified using an antibacterial metalloporphyrin (CuPpIX) sonosensitizer (Scheme 1). Au@BSA-CuPpIX can effectively eliminate *F. nucleatum* and reduce the levels of apoptosis-inhibiting proteins in cancer cells, thus enhancing the tumor therapeutic effect of SDT. In addition, xenograft and orthotopic CRC models demonstrated that Au@BSA-CuPpIX has high SDT efficiency for the effective suppression of tumor growth, and tumor metastases are significantly reduced by eliminating *F. nucleatum* in mice after treatment with antibacterial Au@BSA-CuPpIX. Moreover, Au NPs can reduce or even eliminate the phototoxicity of CuPpIX in the skin by reducing the production of light-induced ROS and avoiding severe inflammation and skin damage. This study offers a reference that ensures efficient treatment of tumors while minimizing side effects.

RESULTS AND DISCUSSION

Synthesis and Characteristics of Au@BSA-CuPpIX. For the efficient SDT of CRC with reduced phototoxic skin injury, an antibacterial nanoplatform (Au@BSA-CuPpIX) was synthesized by BSA anchoring Au NPs and modified using metalloporphyrin (CuPpIX). The uniform morphology of the fabricated Au@BSA-CuPpIX was revealed through transmission electron microscopy (TEM) imaging (Figure 1a) and in terms of the high angle annular dark field (HAADF) image. The morphology of Au@BSA-CuPpIX presented a spherical monodispersion, consistent with TEM (Figure 1b). Elemental mapping analysis shows Cu and Au were uniformly distributed in the Au@BSA-CuPpIX, which substantiated the chemical composition of Au@BSA-CuPpIX (Figure 1c–e). The energy dispersive spectrometer (EDS) analysis confirmed the presence of the elements Au and Cu, indicating that Au NPs and CuPpIX payloads onto the BSA (Figure 1f). The mean hydrodynamic diameter of Au@BSA-CuPpIX was about 53 nm (Figure 1g). The UV–vis absorption spectrum of Au@BSA-CuPpIX exhibited broader characteristic absorption bands between 350–420 nm and 550–600 nm compared to Au@BSA, which can be attributed to the presence of CuPpIX in Au@BSA-CuPpIX (Figure 1h). After grafting CuPpIX onto Au@BSA, the zeta potential reduced to −48.26 ± 1.107 mV (Figure 1i). From the stability of Au@BSA-CuPpIX in a serum-containing medium, its particle size did not change significantly over time, indicating its good stability in the physiological environment (Figure S1). Owing to the successful loading of CuPpIX, Au@BSA-CuPpIX could be utilized to be a sonosensitizer for generating singlet oxygen ($^1O_2$) for tumor treatment. Single oxygen sensor green (SOSG), which is known as a fluorescent probe showing a high specificity for $^1O_2$, was applied to evaluate the capability of Au@BSA-CuPpIX to generate $^1O_2$ (Figure 1j). SOSG fluorescence was more intense in the Au@BSA-CuPpIX+US

https://doi.org/10.1021/acsnano.3c01308
ACS Nano 2023, 17, 11466–11480

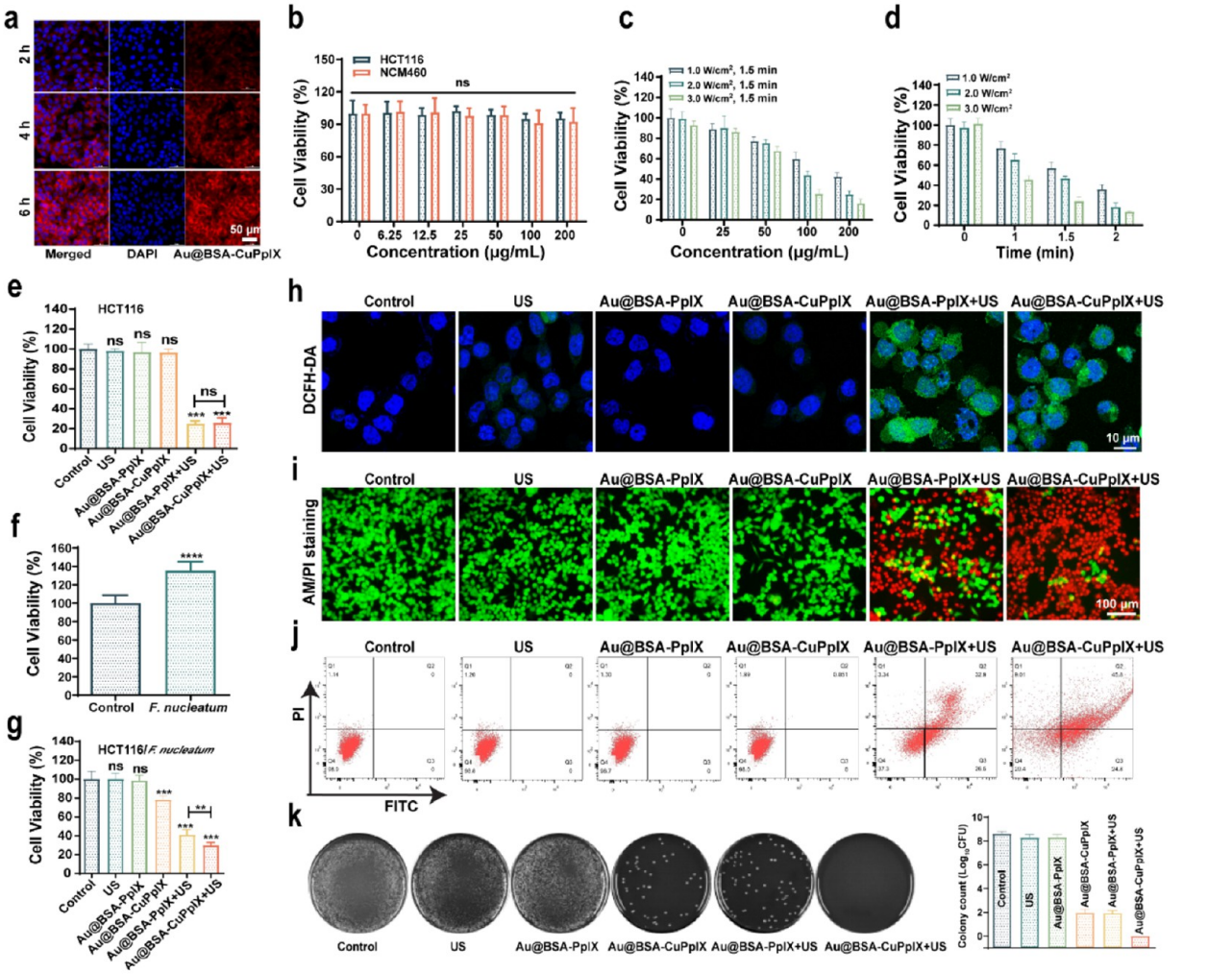

Figure 3. *In vitro* **anticancer and antibacterial activities. (a) CLSM pictures of HCT116 cells after being co-incubated with Au@BSA-CuPpIX for 2, 4, and 6 h. Red fluorescence: Cy5.5-labeled Au@BSA-CuPpIX (100 μg/mL), blue fluorescence: DAPI. (b) The viabilities of HCT116 and NCM460 cells after incubation with Au@BSA-CuPpIX for 24 h at different concentrations (0, 6.25, 12.5, 25, 50, 100, and 200 μg/mL). (c) Cell viabilities of HCT116 cells treated with Au@BSA-CuPpIX at varied concentrations (0, 25, 50, 100, and 200 μg/mL) using varying power densities (1.0, 2.0, and 3.0 W/cm^2) of US irradiation. (d) The viability of HCT116 cells under varying US irradiation durations (0, 1, 1.5, 2 min) or different power densities (1.0, 2.0, 3.0 W/cm^2) while being treated by Au@BSA-CuPpIX at a concentration of 100 μg/mL. (e) The viability of HCT116 cells evaluated after various treatments (PBS, Au@BSA-PpIX, Au@BSA-CuPpIX, US, Au@BSA-PpIX+US, Au@BSA-CuPpIX+US). (f) The cell viabilities of HCT116 cells after coculture with *F. nucleatum* (1:1000) after 48 h. (g) Cocultured with *F. nucleatum* after 48 h, the cell viability of HCT116 cells after different treatments. (h) Images of HCT116 cells obtained through CLSM after various treatments stained with DCFH-DA. (i) Images captured through inverted fluorescence microscopy images of HCT116 cells that have been stained by Calcein-AM and PI dyes in different treatments (green fluorescence: Calcein-AM representing live cells, red fluorescence: PI representing dead cells). (j) Cocultured with *F. nucleatum* after 48 h, flow cytometric analysis of HCT116 cells after various treatments. (k) Plate photographs of *F. nucleatum* forming a colony after different treatments. The corresponding colony count results of different treatment groups.**

group in comparison with the fluorescence in the Au@BSA-CuPpIX group, indicating that Au@BSA-CuPpIX produced sufficient $^1O_2$ excited by US. The singlet oxygen production efficiency of Au@BSA-CuPpIX and Au@BSA-PpIX under US irradiation showed no obvious differences. The production of $^1O_2$ was detected through using electron spin resonance (ESR) (Figure 1k). The ESR results showed a strong characteristic 1:1:1 triple peak of $^1O_2$ in the Au@BSA-CuPpIX+US and Au@BSA-PpIX+US groups, demonstrating that Au@BSA-CuPpIX can be used as an effective sonosensitizer to produce $^1O_2$. To evaluate the ability of Au NPs to inhibit the production of light-induced ROS, the ROS production efficiency of Au@BSA-CuPpIX and BSA-CuPpIX was measured using SOSG (Figure 1l). The findings showed that the group treated with Au@BSA-CuPpIX demonstrated a 76% decrease in ROS production efficiency compared to that in the BSA-CuPpIX group under photoradiation conditions, indicating that entrapping Au NPs in Au@BSA-CuPpIX could effectively reduce the generation of light-induced ROS. Therefore, Au@BSA-CuPpIX is expected to effectively reduce the phototoxicity of sonosensitizers to the skin during tumor therapy. Considering that Au NPs have displayed a shielding effect of Au NPs on light-induced ROS production, further investigation was carried out on the ROS production effect of Au NPs induced by US radiation. The SOSG and ESR results suggested that the efficiency of ROS production was reduced

https://doi.org/10.1021/acsnano.3c01308
ACS Nano 2023, 17, 11466−11480

by 48.3% in the Au@BSA-CuPpIX group when compared to the BSA-CuPpIX group (Figures S2, S3). Au NPs revealed a more notable effect on light-triggered ROS production than that on sound-induced ROS production (76% *vs* 48.3%, respectively). This difference could be attributed to the different mechanisms of ROS generation excited by light and US.[23] Therefore, Au@BSA-CuPpIX is promising for tumor SDT while overcoming phototoxicity in the skin.

Au@BSA-CuPpIX Effective Elimination of *F. nucleatum*. To investigate the *in vitro* antibacterial properties of Au@BSA-CuPpIX, *F. nucleatum* was co-incubated with phosphate-buffered saline (PBS), Au@BSA-CuPpIX, and Au@BSA-PpIX suspensions for 24 h in the dark at a certain dosage (100 μg/mL). According to bacterial viability, colony images, and colony count results (Figure 2a,b), Au@BSA-CuPpIX could significantly eliminate *F. nucleatum*, highlighting its efficient antibacterial properties, which was attributed to the addition of CuPpIX. The antibacterial ability of Au@BSA-CuPpIX was attributed to the antibacterial property of CuPpIX. The antibacterial activity of $^1O_2$ produced by US-excited sonosensitizers was then evaluated. The growth of *F. nucleatum* treated with Au@BSA-PpIX was above 90%. However, after Au@BSA-PpIX was irradiated by the US, the survival rate of *F. nucleatum* sharply decreased, demonstrating that US-triggered $^1O_2$ production also possessed antibacterial activity. Although Au@BSA-PpIX combined with US irradiation showed antibacterial activity, the Au@BSA-CuPpIX group with US irradiation showed a stronger inhibition of *F. nu*cleatum proliferation, indicating that Au@BSA-CuPpIX had the synergistic antibacterial ability of both CuPpIX and $^1O_2$. The cocultured *F. nucleatum* was sampled, dehydrated, fixed, and sectioned for scanning electron microscopy (SEM) (Figure 2c). Correspondingly, compared with the control and Au@BSA-PpIX groups with or without US radiation, bacterial dehydration and bacterial membrane contraction could be clearly observed in the group treated with Au@BSA-CuPpIX with US radiation, which was in agreement with the colony forming ability results. The antibacterial ability of Au@BSA-CuPpIX was assessed by staining for live/dead bacteria (Figure 2d). As expected, in the absence of US radiation, the control and Au@BSA-PpIX groups emitted only green fluorescence, indicating that *F. nucleatum* was viable. However, Au@BSA-PpIX treatment in the presence of US radiation resulted in some dead bacteria (emitting red fluorescence), which may have been due to the SDT effect of Au@BSA-PpIX. Moreover, numerous dead bacteria (emitting red fluorescence) were observed in the Au@BSA-CuPpIX treatment with or without US radiation, indicating that Au@BSA-CuPpIX had strong antibacterial activity.

Cellular Uptake, Biocompatibility, and SDT Efficiency of Au@BSA-CuPpIX *in Vitro*. First, the uptake of Au@BSA-CuPpIX labeled with cyanine (Cy)5.5 dye in cells was observed by confocal laser scanning microscopy (CLSM). The endocytosis of Au@BSA-CuPpIX into HCT116 cells was successfully demonstrated (Figure 3a). Next, to assess the biocompatibility of Au@BSA-CuPpIX, the cell viability of human cells (HCT116 and NCM460), incubated with Au@BSA-CuPpIX at different concentrations (6.25, 12.5, 25, 50, 100, and 200 μg/mL) for 24 h, was determined by the cell counting kit-8 (CCK-8). The results showed that Au@BSA-CuPpIX exhibited no obvious toxicity, even at high concentrations (up to 200 μg/mL) (Figure 3b). Owing to the good compatibility and efficient phagocytosis, the SDT efficiency of Au@BSA-CuPpIX *in vitro* was investigated using CCK-8. The concentration of Au@BSA-CuPpIX, US power density, and US irradiation duration showed a negative correlation with cell viability (Figure 3c,d), demonstrating that Au@BSA-CuPpIX had a high sonotoxicity efficiency. It is noteworthy that there was no apparent variation observed in the SDT efficiency under US radiation when cells were cocultured with Au@BSA-PpIX and Au@BSA-CuPpIX (Figure 3e), indicating no significant difference between the sonotoxicity of Au@BSA-CuPpIX and Au@BSA-PpIX in killing uninfected HCT116 cells.

The impact of *F. nucleatum* on the growth of HCT116 cells was explored. It was found that there was an obvious increase in HCT116 cell proliferation following a 48 h incubation with *F. nucleatum* at a concentration of 1:1000 (Figure 3f), which is consistent with previous reports.[16,51,52] Then, *F. nucleatum*-infected HCT116 cells were used to evaluate the effect of SDT combined with an antibacterial. As shown in Figure 3g, after US irradiation, Au@BSA-CuPpIX exhibited a more obvious inhibitory effect on cell viability than Au@BSA-PpIX, suggesting that the sonotoxicity of Au@BSA-CuPpIX for *F. nucleatum*-infected tumor cells was stronger than that of Au@BSA-PpIX, which could be attributed to the stronger antibacterial ability of Au@BSA-CuPpIX to eliminate *F. nucleatum*. The levels of TLR4 and MyD88 proteins could be enhanced in HCT116 in response to the treatment of *F. nucleatum*, leading to sustained activation of NF-κB. Western blot was used to explore the effect of Au@BSA-CuPpIX on this pathway after eliminating *F. nucleatum* (Figure S4). The findings indicated that TLR4, MyD88, and p65 levels remained unchanged in the control group. However, these proteins were noticeably decreased in the Au@BSA-CuPpIX and Au@BSA-CuPpIX+US groups. This could be attributed to the exceptional antibacterial properties of Au@BSA-CuPpIX, which may have prevented the TLR4/MyD88/NF-κB pathway from being activated. Previous reports have found that intratumoral *F. nucleatum* may reduce the effectiveness of CRC treatment through microbial metabolites or activation of apoptosis suppressor genes. Therefore, Western blot was used to analyze the mechanism of eliminating *F. nucleatum* to enhance ROS-induced apoptosis (Figure S5). The results indicated that the Au@BSA-CuPpIX+US group showed a significant rise in the levels of apoptosis-promoting proteins (cleaved caspase 3, cleaved caspase 9, and Bax) and a decline in the apoptosis-inhibiting protein (Bcl-2). Interestingly, although apoptosis-promoting proteins in the Au@BSA-CuPpIX group did not increase compared to those in the control group, the level of the apoptosis-inhibiting protein Bcl-2 was obviously decreased, indicating that the apoptosis-inhibiting protein Bcl-2 was down-regulated by eliminating *F. nucleatum*. The elevated intracellular ROS induced by Au@BSA-CuPpIX irradiated with US was detected using 2,7-dichlorofluorescein diacetate (DCFH-DA), which could be oxidized by ROS from the nonfluorescent state to fluorescent 2,7-dichlorofluorescein (DCF). As shown in with US irradiation, Au@BSA-CuPpIX and Au@BSA-PpIX generated intense green fluorescence in cancer cells, indicating massive production of intracellular ROS (Figure 3h).

CLSM images were used to verify the therapeutic function of the Au@BSA-CuPpIX. HCT116 cells were cocultured with *F. nucleatum* (1:1000 dilution). Calcein-acetoxymethyl ester (Calcein-AM) and propidium iodide (PI) were costained with HCT116 cells in all groups after treatment to differentiate

https://doi.org/10.1021/acsnano.3c01308
ACS Nano 2023, 17, 11466−11480

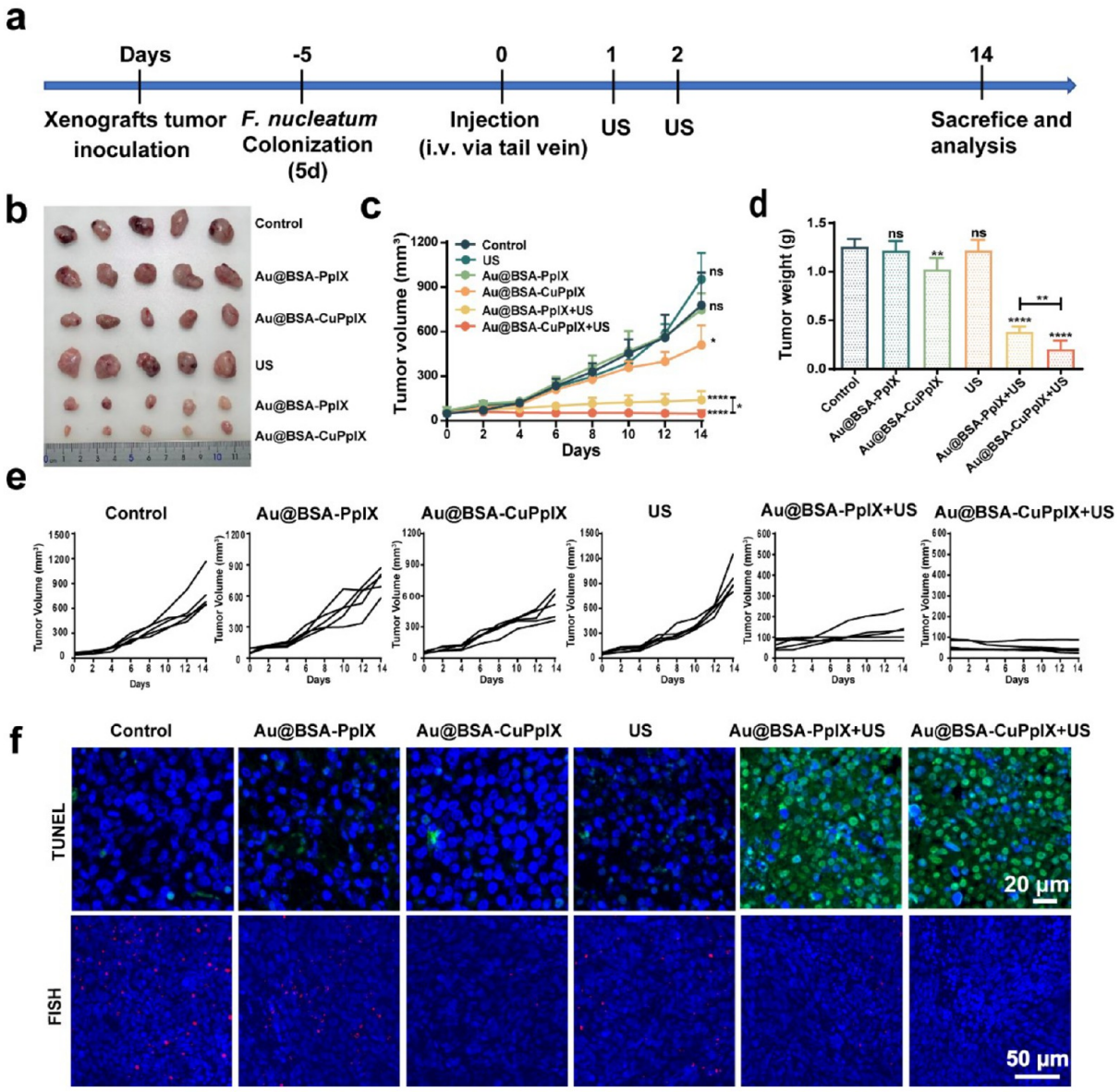

Figure 4. SDT efficiency of Au@BSA-CuPpIX *in vivo*. (a) Schematic illustration of experimental design and schedule of treatments. (b) Photograph of mouse tumors and (c) tumor growth volume curves at the end of the treatments (PBS, Au@BSA-PpIX, Au@BSA-CuPpIX, US, Au@BSA-PpIX+US, Au@BSA-CuPpIX+US). (d) Average tumor weight in different groups. (e) Individual tumor growth curve in different groups. (f) Representative fluorescent TUNEL and FISH-stained sections of HCT116 tumor tissue at the end of the experiments.

between live (green fluorescent) and dead (red fluorescent) cells. Strong green fluorescence and weak red fluorescence were observed in the control, US, Au@BSA-PpIX, and Au@BSA-CuPpIX groups, suggesting good biocompatibility in HCT116 cells. Notably, after US irradiation, the Au@BSA-PpIX+US group and Au@BSA-CuPpIX+US group showed strong red fluorescence originating from PI, which indicated significant cell death (Figures 3i, S6). The use of flow cytometry helped in further evaluating the rate of apoptosis. The control, US, Au@BSA-PpIX, and Au@BSA-CuPpIX groups showed no obvious apoptotic rates. Under US irradiation, the highest apoptosis rate was approximately 70% in the Au@BSA-CuPpIX+US group (Figure 3j). These results, together with the CCK8 results, further demonstrate that the antibacterial and SDT effects of Au@BSA-CuPpIX played a synergistic role in inhibiting cell viability. The bactericidal ability of Au@BSA-CuPpIX against *F. nucleatum* cocultured with cells was investigated further. HCT116 cells from the various treatments described above were lysed with 0.1% Triton X-100 for CFU counting. Au@BSA-CuPpIX could effectively inhibit the growth of *F. nucleatum* cocultured with cells, while Au@BSA-CuPpIX almost completely eliminated *F. nucleatum* after US irradiation (Figure 3k). It can be inferred from the results that the use of Au@BSA-CuPpIX in tandem with US has the potential to effectively eliminate *F. nucleatum*, thus augmenting SDT for CRC.

***In Vivo* Biocompatibility and Biodistribution of Au@BSA-CuPpIX.** Prior to the *in vivo* assessment, the red blood cell hemolysis assay of Au@BSA-CuPpIX was performed, and no significant hemolysis was detected, indicating the benign hemocompatibility of Au@BSA-CuPpIX (Figure S7a,b). To assess the biocompatibility of Au@BSA-CuPpIX *in vivo*,

https://doi.org/10.1021/acsnano.3c01308
ACS Nano 2023, 17, 11466−11480

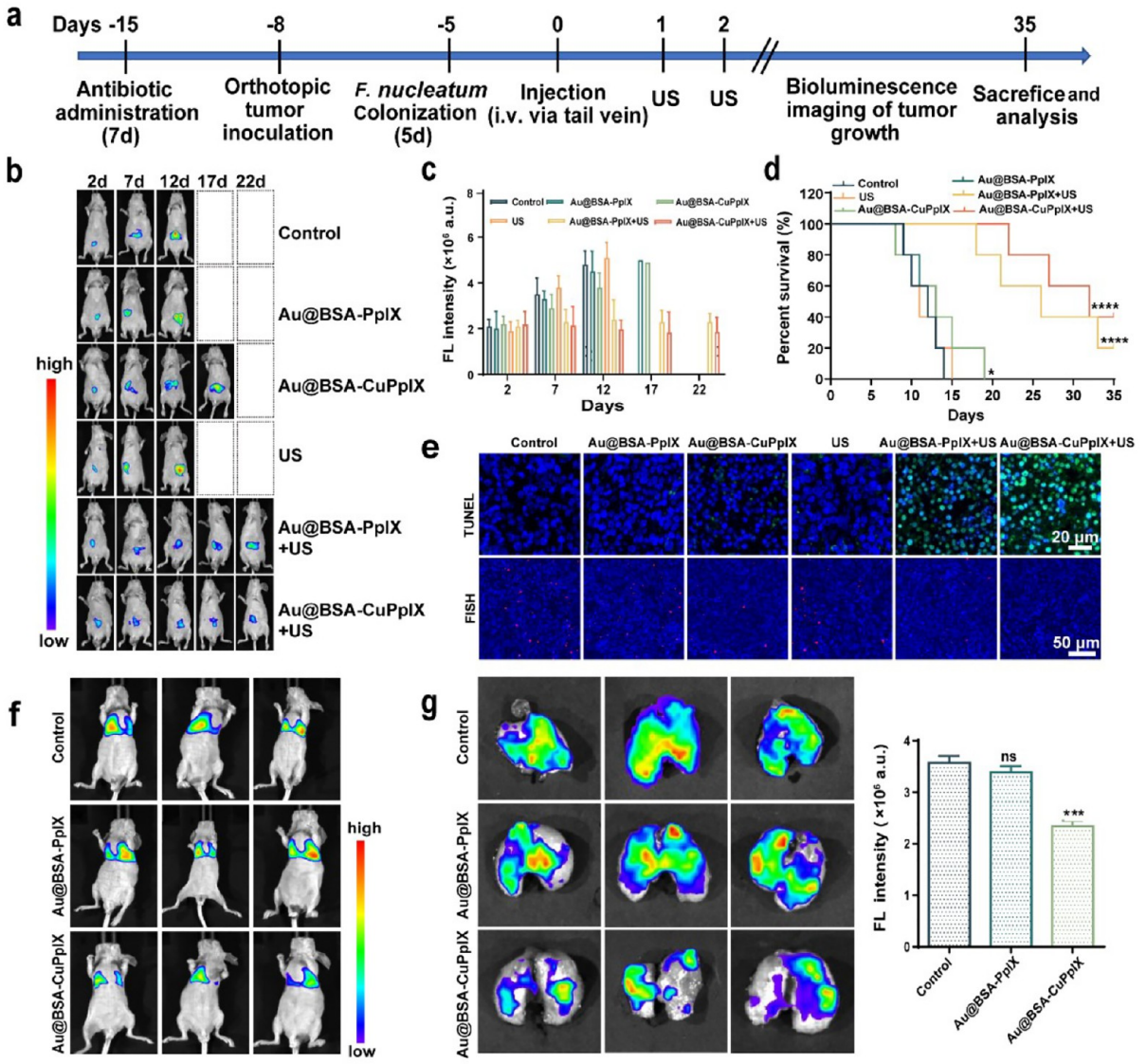

Figure 5. ***In vivo*** **SDT of Au@BSA-CuPpIX against** ***F. nucleatum*****-infected orthotopic CRC and lung metastasis. (a) Schematic illustration of experimental design and treatment regimen. (b) Representative fluorescence images of** ***in vivo*** **bioluminescence imaging of orthotopic HCT116-Luc tumor-bearing mice with different treatments at 35 d (*n* = 5). (c) The corresponding quantitative evaluation for bioluminescence imaging of orthotopic HCT116-Luc tumor-bearing mice with different treatments at 35 d (*n* = 5). (d) Survival rates of mice receiving different treatments were plotted over a period of 35 d (*n* = 5) to evaluate the therapeutic efficacy. (e) Representative fluorescence images of TUNEL and FISH-stained sections at the end of the experiments. (f)** ***In vivo*** **fluorescence intensities of lung metastasis. (g)** ***Ex vivo*** **fluorescence imaging of the lung and fluorescence intensity after treatments.**

healthy male mice were injected intravenously with different amounts of Au@BSA-CuPpIX (0, 5, 10, and 20 mg/kg). Mice in all groups did not significantly lose body weight during the observation period (14 d), indicating that Au@BSA-CuPpIX was not acutely toxic (Figure S8). Furthermore, Au@BSA-CuPpIX showed negligible toxicity to treated mice at different doses, as confirmed by blood biochemical analysis and histological examination (Figures S9, S10). These preliminary data suggest that the synthesized Au@BSA-CuPpIX was highly biocompatible *in vivo*.

To evaluate the biodistribution of Au@BSA-CuPpIX *in vivo*, Cy5.5-labeled Au@BSA-CuPpIX were intravenously injected into mice. The biodistribution of Cy5.5-labeled Au@BSA-CuPpIX was assessed using an *in vivo* imaging system (IVIS). The results indicated that the liver, lung, and kidney had the highest accumulation of Au@BSA-CuPpIX (Figure S11). The quantities of Au NPs in the important organs were measured by utilizing inductively coupled plasma atomic emission spectrometry (ICP-AES), and the results indicated that the major organs where the Au@BSA-CuPpIX were found to accumulate were the liver, lung, spleen, and kidney (Figure S12). Forty-eight hours after injection, the quantity of Au NPs in the tumor increased by 2.97 times compared to 2 h postinjection, indicating the effective tumor accumulation of Au@BSA-CuPpIX through the enhanced permeability and retention effect. The blood circulation curve results showed that the blood circulation half-life of the albumin-based nanoparticles was 31.0 ± 5.9 h, which further verified the stability of the albumin-based nanoplatform *in vivo* (Figure S13).

In Vivo SDT of Au@BSA-CuPpIX against *F. nucleatum*-Infected Tumor-Bearing Xenograft and Orthotopic

https://doi.org/10.1021/acsnano.3c01308
ACS Nano 2023, 17, 11466−11480

CRC. As high *F. nucleatum* levels are strongly associated with the progression of CRC, eliminating *F. nucleatum* is beneficial for promoting therapeutic efficacy. Due to the high ROS yield and the strong antibacterial activity of Au@BSA-CuPpIX, the efficacy of antibacterial synergistic tumor SDT *in vivo* was further investigated in HCT116 cell tumor xenografts and orthotopic CRC-bearing nude mice. First, mice bearing HCT116 tumor xenografts were constructed. Mice were allocated into six groups at random: control, Au@BSA-PpIX, Au@BSA-CuPpIX, US, Au@BSA-PpIX+US, and Au@BSA-CuPpIX+US. To construct the *F. nucleatum*-infected HCT116 cell tumor xenografts, each group of mice received an intratumoral injection of the same amount of *F. nucleatum* (10^9 CFUs per mouse) every day for a total of 5 d of colonization, as previously described.[47] Then, PBS, Au@BSA-PpIX, and Au@BSA-CuPpIX were injected intravenously 24 h after the last *F. nucleatum* injection, followed 24 h later by irradiation of the tumor with US, repeated the next day (Figure 4a). The growth of tumors was inhibited in the Au@BSA-CuPpIX group compared to the control and Au@BSA-PpIX groups, suggesting that antibacterial Au@BSA-CuPpIX could inhibit tumor growth by eliminating intratumoral *F. nucleatum*. After US irradiation, the Au@BSA-PpIX+US group showed obvious tumor inhibitory effects (82.1%). However, the Au@BSA-CuPpIX+US group had the highest tumor inhibition efficiency (94%) due to the antibacterial combined SDT effect (Figure 4b−e). After the treatment, tumor tissues were harvested from all groups and subjected to histological examination using haematoxylin and eosin (H&E) staining, immunohistochemical (IHC) staining for Ki-67, and TdT-mediated dUTP nick end labeling (TUNEL) staining. Compared with other treatments, H&E staining showed significant lesions in tumor tissues in both Au@BSA-PpIX +US and Au@BSA-CuPpIX+US treatment groups. Moreover, the Au@BSA-CuPpIX+US treatment group demonstrated the most significant suppression of cellular proliferation, as observed by Ki-67 staining. The TUNEL results indicated that the Au@BSA-CuPpIX+US treatment group had a significantly higher number of apoptotic cells with green fluorescence compared to the control groups (Figures 4f, S14). To investigate the inhibitory effect of Au@BSA-CuPpIX on intratumoral *F. nucleatum*, specific fluorescence *in situ* hybridization (FISH) probes with red fluorescence were used to detect *F. nucleatum* in tumors. The results showed that minimal red fluorescence was observed in the Au@BSA-CuPpIX group following US radiation treatment (Figure 4f), indicating that Au@BSA-CuPpIX+US could effectively scavenge intratumoral *F. nucleatum*. These results suggest that Au@BSA-CuPpIX showed superior therapeutic efficacy against xenografted colorectal tumors by eliminating the core oncogenic bacteria combination with SDT.

To investigate the impact of *F. nucleatum* in a clinically relevant model of CRC, *F. nucleatum*-infected HCT116 cells with orthotopic tumor were constructed. First, mice were treated daily with an oral antibiotic mixture (streptomycin and penicillin) for a total of 1 week, and an orthotopic CRC model was established *in vivo* by injecting HCT116 cells transfected with luciferase into the cecum.[53,54] Three days later, mice were administered *F. nucleatum* (10^9 CFUs) by tube feeding every day for a total of 5 d. Other treatments were similar to the xenograft tumor subcutaneously model (Figure 5a). Tumor growth was monitored by bioluminescence every 5 d (Figure 5b). The results of the quantitative analysis of *in vivo* bioluminescence images showed that the bioluminescence intensity of the Au@BSA-CuPpIX group was weaker than that of the control and Au@BSA-PpIX groups, which was related to the antibacterial activity of Au@BSA-CuPpIX. The bioluminescence intensity of Au@BSA-PpIX+US was weak, while the bioluminescence intensity of the Au@BSA-CuPpIX +US treatment group was the weakest, indicating that the antibacterial Au@BSA-CuPpIX had a stronger antitumor response than Au@BSA-PpIX because of the synergy between antibacterial activity and SDT (Figure 5c). Moreover, the survival time of mice was examined in treatment groups over 35 d, showing that all mice died within 35 d in the control, Au@BSA-PpIX, Au@BSA-CuPpIX, and US groups (Figure 5d). As expected, antibacterial activity combined with SDT therapy extended the median survival time and survival rate (>35 d, 40%) compared to antibacterial activity (=19 d, 0%) or SDT therapy alone (>35 d, 20%). In addition, orthotopic tumor tissue was pathologically stained with H&E, Ki-67, and TUNEL, showing that Au@BSA-CuPpIX+US caused the most severe damage to the tumor tissue and induced the most severe apoptosis (Figures 5e, S15). FISH results also showed that Au@BSA-CuPpIX had strong antibacterial activity in orthotopic tumors (Figure 5e), which is in agreement with the results obtained from the tumor xenograft CRC. These findings implied that the proliferation and invasion activity of CRC cell lines could be increased by *F. nucleatum*, and the combination treatment of Au@BSA-CuPpIX and US was found to be effective in suppressing the growth of both tumor xenografts and orthotopic colorectal tumors by clearing *F. nucleatum* synergetic SDT, further illustrating that the elimination of CRC core pathogens is necessary for CRC treatment.

F. nucleatum infection has been reported to promote CRC cell migration and lung metastasis.[55−59] To further explore whether antibacterial Au@BSA-CuPpIX could reduce metastasis *in vivo*, a lung metastasis model was constructed by injecting *F. nucleatum*-infected HCT116 cells overexpressing luciferase *via* the tail vein. Mice were allocated randomly into three groups (control, Au@BSA-PpIX, and Au@BSA-CuPpIX) for different treatments. After 14 d, strong bioluminescence from metastases was detected in the lungs of the PBS and Au@BSA-PpIX groups, which showed higher bioluminescence than that of the antibacterial Au@BSA-CuPpIX group (Figure 5f). These *in vivo* imaging findings were consistent with end-point bioluminescence intensity in lung imaging of euthanized mice (Figure 5g), confirming that tumor metastases were significantly reduced in mice treated with antibacterial Au@BSA-CuPpIX. Therefore, inhibition of *F. nucleatum* by Au@BSA-CuPpIX suppressed CRC metastasis.

Skin Phototoxicity Evaluation. Porphyrins generally cause severe phototoxicity in the skin when exposed to light, which hinders their clinical application.[60−62] Au NPs are superior electron/energy receivers, which could convert the excited singlet state of porphyrins through electron/energy transfer, thereby reducing the formation of the triplet state of porphyrins.[63−68] Energy/electron transfer may occur from CuPpIX to Au NPs under light conditions, which could reduce the ROS production excited by light to prevent porphyrins from damaging the skin. Therefore, engineered Au@BSA-CuPpIX may weaken and even eliminate the phototoxicity of porphyrins to protect skin from damage. To determine the skin protective effect of Au NPs, normal human skin epithelial cells HaCaT were cocultured with Au@BSA-CuPpIX and BSA-

https://doi.org/10.1021/acsnano.3c01308
ACS Nano 2023, 17, 11466−11480

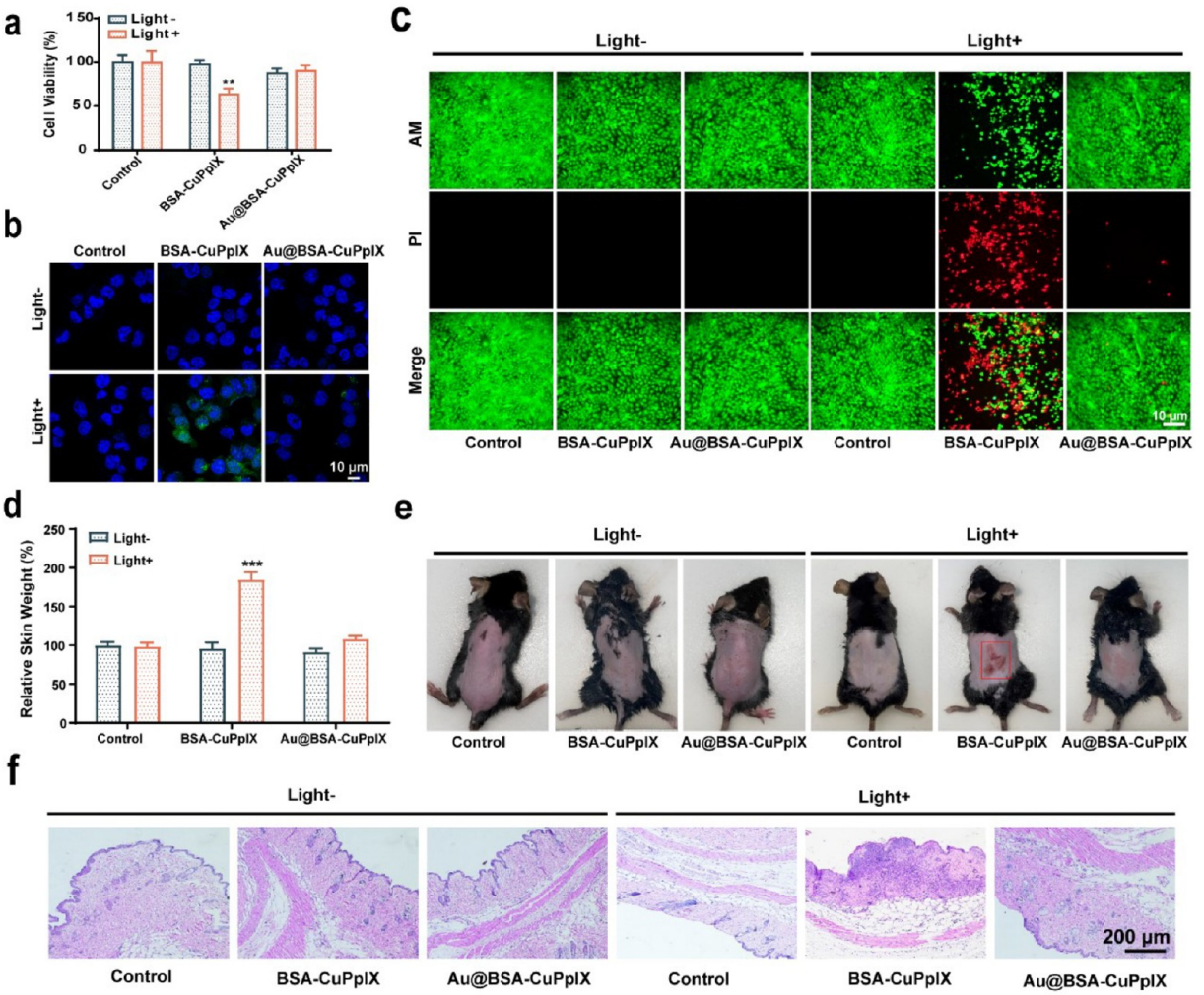

Figure 6. Skin photoprotection evaluation. (a) The viability of HaCaT cells was assessed by CCK8 assay after being cultured with PBS, BSA-CuPpIX, and Au@BSA-CuPpIX, with or without LED light (405 nm) irradiation (5 W/cm^2 for 5 min) at the same CuPpIX concentration. (b) The confocal imaging of HaCaT cells treated with PBS, BSA-CuPpIX, and Au@BSA-CuPpIX and then stained using DCFH-DA (green). The cell nuclei were stained using DAPI (blue). (c) The confocal imaging of live and dead cells stained by Calcein-AM and PI dyes. (d) Skin samples measuring 1.5 cm × 1.5 cm were collected to determine their relative weight after exposing the backs of euthanized mice to 405 nm LED light at a power density of 5 mW/cm^2 for 2 h. (e) Photograph and (f) H&E sections of the skin tissue on the back of the mouse taken 3 days after with or without exposure to 405 nm LED light (5 mW/cm^2, 2 h) treatments.

CuPpIX for 24 h. After irradiation with 405 nm light emitting diode (LED) light for 5 min, cells treated with BSA-CuPpIX showed a low level of cell viability and a high level of ROS (Figure 6a−c). However, cells treated with the same concentration of Au@BSA-CuPpIX with or without light irradiation had a minimal effect on cell viability and low level of ROS production, indicating no obvious phototoxicity of Au@BSA-CuPpIX.

Furthermore, the protective effect of Au NPs against porphyrin skin phototoxicity was assessed in shaved, healthy male C57BL/6 mice. After intravenous injection of PBS, BSA-CuPpIX, and Au@BSA-CuPpIX for 24 h, the mice were irradiated with or without 405 nm LED light for 2 h to evaluate the photodamage of the dorsal skin of mice. Skin damage in mice was negligible in the group without light irradiation. After illumination, the mice injected with BSA-CuPpIX showed significant edema on their backs. However, mice administered Au@BSA-CuPpIX injection did not show significant edema of the skin after light irradiation. To quantify the skin edema of mice receiving different treatments, skin samples measuring 1.5 cm × 1.5 cm were collected from the backs of three euthanized mice in each group and weighed. It is worth noting that the mean skin weight of mice receiving BSA-CuPpIX combined with illumination was approximately 180% greater than that of mice in the control group, whereas there was no significant change in skin weight after treatment with Au@BSA-CuPpIX combined with illumination, indicating that Au NPs eliminated the phototoxicity of porphyrins on the skin (Figure 6d). Moreover, severe edema in mice treated with BSA-CuPpIX combined with illumination gradually developed into erythema and eschar. Severe skin erythema was observed on the backs of mice treated with BSA-CuPpIX combined with illumination at day 3, whereas mice treated with Au@BSA-CuPpIX combined with illumination had no significant erythema (Figure 6e). Histological changes in the skin were evaluated 3 days after light irradiation using H&E staining. Mice treated with BSA-CuPpIX showed severe skin damage following light irradiation. In sharp contrast, the skin of the mice treated with Au@BSA-

https://doi.org/10.1021/acsnano.3c01308
ACS Nano 2023, 17, 11466−11480

CuPpIX remained essentially intact after irradiation (Figure 6f). Taken together, all these results suggest that Au@BSA-CuPpIX reduced the severe phototoxicity of sonosensitizers, highlighting a promising approach offering a sonosensitizer with efficiency, precision, and biosafety.

CONCLUSION

In this study, we constructed an ultrasmall antibacterial nanoplatform (Au@BSA-CuPpIX), which made it easy for it to be metabolized by the kidney. Au@BSA-CuPpIX exhibited good ultrasonic-excited ROS production and antibacterial activity of *F. nucleatum*. The xenografts and orthotopic CRC model *in vivo* experiments showed that Au@BSA-CuPpIX significantly improved the therapeutic effect of SDT and suppressed CRC tumor metastasis by eliminating the pathogenic bacterium *F. nucleatum*. Notably, Au@BSA-CuPpIX reduced the phototoxicity of sonosensitizers and improved their clinical translational potential. Such concepts of "anti-harmful bacteria synergism tumor treatment" are expected to provide a solution and scientific support for accurate and efficient pathogen-related cancer therapies.

MATERIALS AND METHODS

Materials and Reagents. BSA, *N*-hydroxysuccinimide (NHS), *N*-(3-(dimethylamino)propyl)-*N*-ethylcarbodiimide hydrochloride (EDC), sodium hydroxide, $HAuCl_4{\cdot}4H_2O$, PpIX, CuPpIX, DAPI, 2,2,6,6-tetramethylpiperidine (TEMP), DCFH-DA, Calcein acetoxymethyl ester (Calcein-AM), and propidium iodide (PI) were purchased from Sigma-Aldrich Inc. CCK-8 was obtained from Beyotime Biotechnology.

Synthesis of Protein-Based Sonosensitizers. BSA was dissolved in ultrapure water, and chloroauric acid ($HAuCl_4{\cdot}4H_2O$) was added dropwise under gentle stirring for 30 min; then a reducing agent (sodium borohydride) was added. After 1 h of reaction, the product underwent a purification process using an ultrafiltration method with a membrane filter (MWCO, 10 kDa), followed by three rounds of water washing, and albumin-stable gold particles (Au@BSA) were obtained. Further, a solution of dimethyl sulfoxide was used to dissolve metal protoporphyrin (CuPpIX) or protoporphyrin (PpIX), and then EDC and NHS were added to the solution and stirred, then added dropwise to the Au@BSA solution and reacted at low temperature for 24 h in the dark. Finally, albumin-complex particles (Au@BSA-CuPpIX or Au@BSA-PpIX) were acquired through ultrafiltration utilizing a 10 kDa membrane filter and subsequently washed with water three times.

Characterization of Protein-Based Sonosensitizer. TEM was performed using a JEM-2100F electron microscope at a working voltage of 200 kV. A UV-3101PC Shimadzu spectrometer was used to measure the UV−vis spectra. A Zetasizer Nanoseries instrument (Nano ZS90) was used to measure the zeta potential and size distribution. An FV 1000 camera (Olympus) was used to collect CLSM images. An ultrasonic transducer (Chattanooga Co., USA) was used in all experiments. A Bruker EMX electron paramagnetic resonance system was used for the ESR.

ESR Test for $^1O_2$. $^1O_2$ production by Au@BSA-CuPpIX, BSA-CuPpIX, and Au@BSA-PpIX was detected using TEMP. Typically, in the presence of TEMP, Au@BSA-CuPpIX, BSA-CuPpIX, and Au@BSA-PpIX (100 μg/mL) solution was subjected to US radiation at a frequency of 1.0 MHz, intensity of 3.0 W/cm^2, and 50% duty cycle for a duration of 120 s. An ESR spectrometer immediately detected the $^1O_2$ signals. The control, Au@BSA-CuPpIX+TEMP, BSA-CuPpIX +TEMP, Au@BSA-PpIX+TEMP, and US+TEMP groups were tested for comparison.

SOSG Test for $^1O_2$. To evaluate the production of singlet oxygen ($^1O_2$), a fluorescent probe called SOSG was utilized. The grouping used in the ESR was replicated, and the fluorescence of the sample was measured at 30 s intervals with or without ultrasonic irradiation. The fluorescence spectrophotometer used was a Shimadzu RF-5301 PC from Japan, with excitation and emission wavelengths set at 488/525 nm. To detect $^1O_2$ produced by light, SOSG was employed. The fluorescence of Au@BSA-CuPpIX and BSA-PpIX (at 100 μg/mL concentration each) was measured at 60 s intervals following light radiation (at 405 nm) for 300 s.

Bacterial Culture. The strain *F. nucleatum* ATCC 25586 was sourced from the American Type Culture Collection and grown in an anaerobic incubator at 37 °C on Columbia blood agar enriched with 5 mg/mL heme, 5% defibrinated sheep blood, and 1 mg/mL vitamin K1 (Sigma-Aldrich).

Evaluation of Antibacterial Activity. *F. nucleatum* (10^9 CFUs/mL, 1 mL) was co-incubated with PBS, Au@BSA-PpIX, or Au@BSA-CuPpIX at a dose of 100 μg/mL for 24 h, followed by US (1.0 MHz, 3.0 W/cm^2, 50% duty cycle) or without US radiation, and the absorbance values of the bacterial suspensions at OD 600 nm were measured from an enzymatic label. The bacterial suspensions of the above groups were taken and then continuously diluted 10^5 times, and the bacterial suspension diluted with 100 μL was spread on an agarose plate. The antibacterial efficacy of Au@BSA-CuPpIX was assessed using the plate counting method. The number of bacterial colonies was observed after incubation at 37 °C for 5 d. Bacterial suspensions from the above groups were collected by centrifugal washing. For SYTO-9/PI staining, dead/live SYTO-9/PI dye was added to the bacteria and incubated for 30 min, washed thrice with PBS, and observed by CLSM. For SEM imaging, the bacteria were fixed in glutaraldehyde and observed.

Coculture Experiment. HCT116 cells were treated with *F. nucleatum* (1:1000) under normal culture conditions for CRC cell lines.

Endocytosis Observed by CLSM. HCT116 cells were seeded onto CLSM dishes (35 mm × 10 mm, Corning Inc., New York) at a density of 1×10^5 and incubated for 12 h. The medium was subsequently replaced with Cy5.5-labeled Au@BSA-CuPpIX (100 μg/mL in DMEM, 1 mL) and further cultured for 2, 4, and 6 h. The nuclei were stained with DAPI before observing the cells using CLSM after a 15 min staining period.

***In Vitro* $^1O_2$ Generation.** The cells were cocultured with Au@BSA-CuPpIX (100 μg/mL) and Au@BSA-PpIX (100 μg/mL) at 37 °C for a period of 6 h. Next, US irradiation (1.0 MHz, 3.0 W/cm^2, 50% duty cycle, 1.5 min) was applied to the cells. After substituting the medium with DCFH-DA (100 μL, $V_{DCFH\text{-}DA}$:V_{DMEM} = 1:9), the cells were stained for an additional 15 min. The cells were thoroughly rinsed with PBS three times and subsequently analyzed using CLSM.

Observation of the Sonotoxicity of Au@BSA-CuPpIX. The protocol for treating the cells is akin to the previously mentioned CLSM observation of $^1O_2$ generation, with the sole exception being that Calcein-AM (2 μM) and PI (4 μM) were used instead of DCFH-DA to stain live and dead cells correspondingly.

SDT Effectiveness of Au@BSA-CuPpIX *in Vitro*. Approximately 1×10^4 cells/well were seeded in 96-well plates to ensure that HCT116 cells adhered to the plates after 12 h. Subsequently, the cells were treated with varying concentrations of Au@BSA-CuPpIX and incubated for 24 h. After 90 min, cell viability was determined *via* a microplate reader by substituting the medium with CCK-8 medium (100 μL, $V_{CCK\text{-}8}$:V_{DMEM} = 1:9), and the absorbance was measured at 450 nm. To investigate the efficiency of SDT combined with its antibacterial activity against cancer cells, the cells were first cocultured with *F. nucleatum* (1:1000) for 48 h, and PBS, Au@BSA-CuPpIX, and Au@BSA-PpIX were added to each group. After irradiation with or without US for 1.5 min (1.0 MHz, 3.0 W/cm^2, 50% duty cycle), cell viability was tested similar to the CCK8 protocol after further incubation for 3 h.

Cell Apoptosis Assay. Flow cytometry was employed to evaluate cell apoptosis and determine the pro-apoptotic capacity of HCT116 cells across various treatment conditions. Following the coculture of HCT116 cells with *F. nucleatum* for 48 h, PBS, Au@BSA-CuPpIX (100 μg/mL), and Au@BSA-PpIX (100 μg/mL) were added to the medium. After US radiation (1.0 MHz, 3.0 W/cm^2, 50% duty cycle,

https://doi.org/10.1021/acsnano.3c01308
ACS Nano 2023, 17, 11466−11480

1.5 min), apoptosis was assessed through Annexin V-FITC and PI staining, followed by flow cytometry analysis.

Western Blot. RIPA lysis buffer (Beyotime, Jiangsu, China) was utilized to extract total protein from diverse HCT116 cell lines. Equivalent quantities of protein samples were applied to a 10% sodium dodecyl sulfate-polyacrylamide gel to facilitate separation, and subsequently, the partitioned proteins were transferred onto a 0.45 μm nitrocellulose membrane. The membrane was then incubated with 5% skim milk for 1 h and incubated with the following primary antibodies overnight at 4 °C: anti-cleaved caspase 3 (Abcam, 1:1000), anti-cleaved caspase 9 (Cell Signaling Technology, 1:1000), anti-Bax (Cell Signaling Technology, 1:1000), anti-Bcl-2 (Cell Signaling Technology, 1:1000), anti-TLR4 (Cell Signaling Technology, 1:1000), anti-MyD88 (Cell Signaling Technology, 1:1000), anti-p65 (Cell Signaling Technology, 1:1000), and anti-GAPDH (Cell Signaling Technology, 1:5000). Subsequently, the corresponding secondary antibody was added to the membrane and incubated at room temperature for an hour. Protein bands were visualized utilizing a chemiluminescence image analysis system (Tanon, Shanghai, China).

Antibacterial Activity of Au@BSA-CuPpIX in Cell and Bacterial Coculture Models. HCT116 cells were incubated with *F. nucleatum* for 48 h and then treated with PBS, Au@BSA-CuPpIX (100 μg/mL), and Au@BSA-PpIX (100 μg/mL) in the medium for a 24 h period, either with or without US radiation. The supernatant was collected with PBS-lysed cells supplemented with 0.1% Triton X-100, and a 100 μL suspension was taken and spread on an agarose plate. CFUs were counted after incubation at 37 °C for 5 d.

***In Vivo* Biocompatibility Assay.** Male BALB/c nude mice (n = 5 per group) were evaluated. The mice were intravenously injected with Au@BSA-CuPpIX at different doses (5, 10, and 20 mg/kg). A control group of mice was used without any treatment. After 14 days of feeding, the mice were weighed and humanely euthanized, with their blood samples and organs gathered for evaluation, encompassing different blood parameters and H&E staining analysis.

Pharmacokinetics of Au@BSA-CuPpIX. Healthy male rats (n = 3) were injected with 10 mg/kg FITC-labeled Au@BSA-CuPpIX intravenously, and orbital blood was taken at 5 min, 30 min, 1 h, 2 h, 4 h, 6 h, 8 h, 12 h, 24 h, and 48 h after administration. After obtaining serum, the fluorescence intensity of FITC was determined and the corresponding blood drug concentration ratio at each time point was calculated.

***In Vivo* Therapy of Tumor in an Orthotopic CRC Model.** Initially, mice were provided with drinking water containing streptomycin (2000 mg/mL) and penicillin (1 U/mL) for a duration of 1 week. Subsequently, human CRC HCT116 tumor cells with luciferase transfection were implanted into the cecum of BALB/c nude mice, creating an orthotopic CRC model. After 3 d, *F. nucleatum* (10^9 CFUs/mouse) was administered orally once a day for 5 d to colonize in the intestine. Mice with tumors were randomly allocated into six separate groups (five mice per group): control, Au@BSA-PpIX (10 mg/kg), Au@BSA-CuPpIX, US, Au@BSA-PpIX+US, and Au@BSA-CuPpIX+US. Equal volumes of PBS, Au@BSA-PpIX (10 mg/kg), and Au@BSA-CuPpIX (10 mg/kg) were injected intravenously into the mice. After injection for 24 h, the US, Au@BSA-PpIX+US, and Au@BSA-CuPpIX+US groups received US radiation (1.0 MHz, 3.0 W/cm^2, 50% duty cycle, 6 min) every other day twice in a row. The IVIS system (PerkinElmer) was employed to monitor the progression of orthotopic tumors through the bioluminescence emitted by cancer cells. After 35 d, the mice were euthanized and dissected for tumor progression analysis. At the conclusion of the treatment, H&E, TUNEL, and Ki-67 staining methods were applied to the tissues for histological examination. FISH staining was utilized to determine the presence of *F. nucleatum*.

***In Vivo* Therapy of a Xenograft Model.** Male BALB/c nude mice 6 weeks of age were given subcutaneous injections of HCT116 cells (5×10^6) on the right side. The mice were randomly distributed into the subsequent groups: control, Au@BSA-PpIX, Au@BSA-CuPpIX, US, Au@BSA-PpIX+US, and Au@BSA-CuPpIX+US. *F. nucleatum* (10^9 CFUs per mouse) was injected into the tumor within 5 d to achieve colonization. PBS, Au@BSA-PpIX (10 mg/kg), and Au@BSA-CuPpIX (10 mg/kg) were injected intravenously into mice, and this was conducted every alternate day for a total of two sessions. Tumor volume growth was observed every 2 days, and measurements were taken using a vernier caliper, following this equation: volume (mm^3) = (length × width^2)/2. The tissues were dissected, weighed, and stained for histological analysis using H&E, TUNEL, and Ki-67 staining at the end of treatment. FISH staining was employed to determine the abundance of *F. nucleatum*.

***In Vivo* Therapy of a Lung Metastasis Model.** For *in vivo* lung metastasis models, 6-week-old male BALB/c nude mice were constructed as previously reported.[50,51] Luciferase-transfected HCT-116 cells were incubated with *F. nucleatum* (1:1000) for 48 h, and the cell resuspension solution was injected *via* the tail vein (10^6 cells, 100 μL per mouse). Mice were injected with PBS (100 μL per mouse), Au@BSA-CuPpIX (10 mg/kg), and Au@BSA-PpIX (10 mg/kg). After 14 d, bioluminescence of lung metastasis of cancer cells was observed using the IVIS system. Mice were humanely euthanized, followed by the surgical extraction of their lungs. Lung biofluorescence was observed using the IVIS system, and fluorescence intensity was calculated.

FISH. FISH was conducted on paraffin-embedded tissues to identify *F. nucleatum*, following the method described in earlier reports.[53,54] The Cy3-labeled *F. nucleatum* probe (5′-CGCAATA-CAGAGTT & GAGCCCTGC-3′) sequence was synthesized by Sangon Biotech Company (Shanghai, China).

***In Vivo* Phototoxicity of Au@BSA-CuPpIX.** To assess the *in vivo* phototoxicity of Au@BSA-CuPpIX *versus* BSA-CuPpIX, 36 healthy C57BL/6 male mice were randomly allocated into six distinct groups (control, control+light, Au@BSA-CuPpIX, Au@BSA-CuPpIX+light, BSA-CuPpIX, and BSA-CuPpIX+light) for assessments. Two sets of mice received intravenous injections of Au@BSA-CuPpIX, while the other two sets were given intravenous injections of BSA-CuPpIX at an equivalent PpIX dosage. After 24 h, the three groups (control+light, Au@BSA-CuPpIX+light, and BSA-CuPpIX+light) exposed to a 405 nm LED light source with a power density of 5 mW/cm^2 for a duration of 2 h. The other three groups received no light. After 4 h, three mice from each group were euthanized, and their dorsal skin was taken to the nearest dimension (1.5 × 1.5 cm) and weighed. The remaining mice were observed. After light treatment for 3 d, each group of mice was imaged using a digital camera. In addition, the previously outlined protocol for H&E staining was followed to evaluate skin damage caused by light exposure.

Statistical Analysis. Mean ± standard error was used for continuous data. An unpaired or paired t test (t test) was used to compare the mean of two groups of normal distribution measurement data. The ANOVA test was used to compare the mean of normal distribution measurement data. $p < 0.05$ was considered statistically significant ($^*p < 0.05$, $^{**}p < 0.01$, $^{***}p < 0.001$, and $^{****}p < 0.0001$).

ASSOCIATED CONTENT

Supporting Information

The Supporting Information is available free of charge at https://pubs.acs.org/doi/10.1021/acsnano.3c01308.

Characterization of materials in Figures S1−S3; SDT mechanism and efficacy in Figures S4−S6; assessment of biosafety in Figures S7−S10; metabolic distribution *in vivo* in Figures S11 and S13; and immunohistochemistry staining in Figures S14 and S15 (PDF)

AUTHOR INFORMATION

Corresponding Authors

Qian Chen − *Nanomedicine and Intestinal Microecology Research Center, Shanghai Tenth People's Hospital, School of Medicine, Tongji University, Shanghai 200072, China*; Email: chenqian163329@163.com

https://doi.org/10.1021/acsnano.3c01308
ACS Nano 2023, 17, 11466−11480

Yang Zhang − *Precision Medicine Center, Taizhou Central Hospital, Taizhou, Zhejiang 318000, China; Nanomedicine and Intestinal Microecology Research Center, Shanghai Tenth People's Hospital, School of Medicine, Tongji University, Shanghai 200072, China*; Email: zhangyang0202@tongji.edu.cn

Huanlong Qin − *Nanomedicine and Intestinal Microecology Research Center, Shanghai Tenth People's Hospital, School of Medicine, Tongji University, Shanghai 200072, China*; orcid.org/0000-0001-5985-5757; Email: hlongqin@126.com

Authors

Xiao Qu − *Nanomedicine and Intestinal Microecology Research Center, Shanghai Tenth People's Hospital, School of Medicine, Tongji University, Shanghai 200072, China*

Fang Yin − *Nanomedicine and Intestinal Microecology Research Center, Shanghai Tenth People's Hospital, School of Medicine, Tongji University, Shanghai 200072, China*

Manman Pei − *Nanomedicine and Intestinal Microecology Research Center, Shanghai Tenth People's Hospital, School of Medicine, Tongji University, Shanghai 200072, China*

Yuanyuan Zhang − *Nanomedicine and Intestinal Microecology Research Center, Shanghai Tenth People's Hospital, School of Medicine, Tongji University, Shanghai 200072, China*

Shengwei Lu − *Nanomedicine and Intestinal Microecology Research Center, Shanghai Tenth People's Hospital, School of Medicine, Tongji University, Shanghai 200072, China*

Xuelian Zhang − *Nanomedicine and Intestinal Microecology Research Center, Shanghai Tenth People's Hospital, School of Medicine, Tongji University, Shanghai 200072, China*

Ziyuan Liu − *Nanomedicine and Intestinal Microecology Research Center, Shanghai Tenth People's Hospital, School of Medicine, Tongji University, Shanghai 200072, China*

Xinyao Li − *Nanomedicine and Intestinal Microecology Research Center, Shanghai Tenth People's Hospital, School of Medicine, Tongji University, Shanghai 200072, China*

Hangrong Chen − *State Key Laboratory of High Performance Ceramics and Superfine Microstructure, Shanghai Institute of Ceramics, Shanghai 200050, China*; orcid.org/0000-0003-0827-1270

Complete contact information is available at: https://pubs.acs.org/10.1021/acsnano.3c01308

Author Contributions

⊥X.Q., F.Y., and M.P. contributed equally to this work. X.Q., Q.C., and M.P. prepared the Au@BSA-CuPpIX nanoplatform, cellular experiment, writing - original draft. Y.Z., X.L., and S.L. performed the animal experiment, data analysis. Q.C., H.C., and F.Y. wrote, reviewed, and edited. X.Z. and Z.L. performed the cellular experiment, bioinformatics analysis. Q.C., Y.Z., and H.Q. conceived the project. Q.C., Y.Z., and H.Q. supervised the project.

Notes

The authors declare no competing financial interest.

ACKNOWLEDGMENTS

We are grateful to Professor Jianlin Shi (Shanghai Institute of Ceramics, Chinese Academy of Sciences) for discussion and technical support. This work was supported by the National Natural Science Foundation of China (Grant Nos. 81730102, 32271384), Shanghai Basic Research Program (Grant No. 20JC1411702), Shanghai Science and Technology Program (Grant No. 20ZR1456100), Basic Study on Public Projects in Zhejiang Province (Grant No. LGF20H060017), the National Key Research and Development Program of China (Grant No. 2021YFB3801001), China Postdoctoral Science Foundation (Grant No. 2021M702484), Shanghai Postdoctoral Excellence Program (Grant No. 2020382), and Shanghai General Hospital Integrated Traditional Chinese and Western Medicine Special Project (Grant No. ZHYY-ZXYJHZX-202105).

REFERENCES

(1) Ternes, D.; Tsenkova, M.; Pozdeev, V. I.; Meyers, M.; Koncina, E.; Atatri, S.; Schmitz, M.; Karta, J.; Schmoetten, M.; Heinken, A.; Rodriguez, F.; Delbrouck, C.; Gaigneaux, A.; Ginolhac, A.; Nguyen, T. T. D.; Grandmougin, L.; Frachet-Bour, A.; Martin-Gallausiaux, C.; Pacheco, M.; Neuberger-Castillo, L.; Miranda, P.; Zuegel, N.; Ferrand, J. Y.; Gantenbein, M.; Sauter, T.; Slade, D. J.; Thiele, I.; Meiser, J.; Haan, S.; Wilmes, P.; Letellier, E. The gut microbial metabolite formate exacerbates colorectal cancer progression. *Nat. Metab* **2022**, *4* (4), 458−475.

(2) Liu, Y.; Fu, K.; Wier, E. M.; Lei, Y.; Hodgson, A.; Xu, D.; Xia, X.; Zheng, D.; Ding, H.; Sears, C. L.; Yang, J.; Wan, F. Bacterial Genotoxin Accelerates Transient Infection-Driven Murine Colon Tumorigenesis. *Cancer Discov* **2022**, *12* (1), 236−249.

(3) Bell, H. N.; Rebernick, R. J.; Goyert, J.; Singhal, R.; Kuljanin, M.; Kerk, S. A.; Huang, W.; Das, N. K.; Andren, A.; Solanki, S.; Miller, S. L.; Todd, P. K.; Fearon, E. R.; Lyssiotis, C. A.; Gygi, S. P.; Mancias, J. D.; Shah, Y. M. Reuterin in the healthy gut microbiome suppresses colorectal cancer growth through altering redox balance. *Cancer Cell* **2022**, *40* (2), 185−200.

(4) Liu, N. N.; Jiao, N.; Tan, J. C.; Wang, Z.; Wu, D.; Wang, A. J.; Chen, J.; Tao, L.; Zhou, C.; Fang, W.; Cheong, I. H.; Pan, W.; Liao, W.; Kozlakidis, Z.; Heeschen, C.; Moore, G. G.; Zhu, L.; Chen, X.; Zhang, G.; Zhu, R.; Wang, H. Multi-kingdom microbiota analyses identify bacterial-fungal interactions and biomarkers of colorectal cancer across cohorts. *Nat. Microbiol* **2022**, *7* (2), 238−250.

(5) Cheng, Y.; Ling, Z.; Li, L. The Intestinal Microbiota and Colorectal Cancer. *Front Immunol* **2020**, *11*, 615056.

(6) Garrett, W. S. The gut microbiota and colon cancer. *Science* **2019**, *364* (6446), 1133−1135.

(7) Tsoi, H.; Chu, E. S. H.; Zhang, X.; Sheng, J.; Nakatsu, G.; Ng, S. C.; Chan, A. W. H.; Chan, F. K. L.; Sung, J. J. Y.; Yu, J. Peptostreptococcus anaerobius Induces Intracellular Cholesterol Biosynthesis in Colon Cells to Induce Proliferation and Causes Dysplasia in Mice. *Gastroenterology* **2017**, *152* (6), 1419−1433.

(8) Long, X.; Wong, C. C.; Tong, L.; Chu, E. S. H.; Ho Szeto, C.; Go, M. Y. Y.; Coker, O. O.; Chan, A. W. H.; Chan, F. K. L.; Sung, J. J. Y.; Yu, J. Peptostreptococcus anaerobius promotes colorectal carcinogenesis and modulates tumour immunity. *Nat. Microbiol* **2019**, *4* (12), 2319−2330.

(9) Lee, S. A.; Liu, F.; Riordan, S. M.; Lee, C. S.; Zhang, L. Global Investigations of Fusobacterium nucleatum in Human Colorectal Cancer. *Front Oncol* **2019**, *9*, 566.

(10) Hamada, T.; Zhang, X.; Mima, K.; Bullman, S.; Sukawa, Y.; Nowak, J. A.; Kosumi, K.; Masugi, Y.; Twombly, T. S.; Cao, Y.; Song, M.; Liu, L.; da Silva, A.; Shi, Y.; Gu, M.; Li, W.; Koh, H.; Nosho, K.; Inamura, K.; Keum, N.; Wu, K.; Meyerhardt, J. A.; Kostic, A. D.; Huttenhower, C.; Garrett, W. S.; Meyerson, M.; Giovannucci, E. L.; Chan, A. T.; Fuchs, C. S.; Nishihara, R.; Giannakis, M.; Ogino, S. Fusobacterium nucleatum in Colorectal Cancer Relates to Immune Response Differentially by Tumor Microsatellite Instability Status. *Cancer Immunol Res.* **2018**, *6* (11), 1327−1336.

(11) Xia, X.; Wu, W. K. K.; Wong, S. H.; Liu, D.; Kwong, T. N. Y.; Nakatsu, G.; Yan, P. S.; Chuang, Y. M.; Chan, M. W.; Coker, O. O.; Chen, Z.; Yeoh, Y. K.; Zhao, L.; Wang, X.; Cheng, W. Y.; Chan, M. T. V.; Chan, P. K. S.; Sung, J. J. Y.; Wang, M. H.; Yu, J. Bacteria pathogens drive host colonic epithelial cell promoter hyper-

methylation of tumor suppressor genes in colorectal cancer. *Microbiome* **2020**, *8* (1), 108.
(12) Mima, K.; Nishihara, R.; Qian, Z. R.; Cao, Y.; Sukawa, Y.; Nowak, J. A.; Yang, J.; Dou, R.; Masugi, Y.; Song, M.; Kostic, A. D.; Giannakis, M.; Bullman, S.; Milner, D. A.; Baba, H.; Giovannucci, E. L.; Garraway, L. A.; Freeman, G. J.; Dranoff, G.; Garrett, W. S.; Huttenhower, C.; Meyerson, M.; Meyerhardt, J. A.; Chan, A. T.; Fuchs, C. S.; Ogino, S. Fusobacterium nucleatum in colorectal carcinoma tissue and patient prognosis. *Gut* **2016**, *65* (12), 1973−1980.
(13) Rubinstein, M. R.; Wang, X.; Liu, W.; Hao, Y.; Cai, G.; Han, Y. W. Fusobacterium nucleatum promotes colorectal carcinogenesis by modulating E-cadherin/β-catenin signaling via its FadA adhesin. *Cell Host Microbe* **2013**, *14* (2), 195−206.
(14) Gur, C.; Ibrahim, Y.; Isaacson, B.; Yamin, R.; Abed, J.; Gamliel, M.; Enk, J.; Bar-On, Y.; Stanietsky-Kaynan, N.; Coppenhagen-Glazer, S.; Shussman, N.; Almogy, G.; Cuapio, A.; Hofer, E.; Mevorach, D.; Tabib, A.; Ortenberg, R.; Markel, G.; Miklić, K.; Jonjic, S.; Brennan, C. A.; Garrett, W. S.; Bachrach, G.; Mandelboim, O. Binding of the Fap2 protein of Fusobacterium nucleatum to human inhibitory receptor TIGIT protects tumors from immune cell attack. *Immunity* **2015**, *42* (2), 344−355.
(15) Gagliani, N.; Hu, B.; Huber, S.; Elinav, E.; Flavell, R. A. The fire within: microbes inflame tumors. *Cell* **2014**, *157* (4), 776−83.
(16) Yang, Y.; Weng, W.; Peng, J.; Hong, L.; Yang, L.; Toiyama, Y.; Gao, R.; Liu, M.; Yin, M.; Pan, C.; Li, H.; Guo, B.; Zhu, Q.; Wei, Q.; Moyer, M. P.; Wang, P.; Cai, S.; Goel, A.; Qin, H.; Ma, Y. Fusobacterium nucleatum Increases Proliferation of Colorectal Cancer Cells and Tumor Development in Mice by Activating Toll-Like Receptor 4 Signaling to Nuclear Factor-kappaB, and Up-regulating Expression of MicroRNA-21. *Gastroenterology* **2017**, *152* (4), 851−866.
(17) Brennan, C. A.; Clay, S. L.; Lavoie, S. L.; Bae, S.; Lang, J. K.; Fonseca-Pereira, D.; Rosinski, K. G.; Ou, N.; Glickman, J. N.; Garrett, W. S. Fusobacterium nucleatum drives a pro-inflammatory intestinal microenvironment through metabolite receptor-dependent modulation of IL-17 expression. *Gut Microbes* **2021**, *13* (1), 1987780.
(18) Yu, T.; Guo, F.; Yu, Y.; Sun, T.; Ma, D.; Han, J.; Qian, Y.; Kryczek, I.; Sun, D.; Nagarsheth, N.; Chen, Y.; Chen, H.; Hong, J.; Zou, W.; Fang, J. Y. Fusobacterium nucleatum Promotes Chemoresistance to Colorectal Cancer by Modulating Autophagy. *Cell* **2017**, *170* (3), 548−563.
(19) Salvucci, M.; Crawford, N.; Stott, K.; Bullman, S.; Longley, D. B.; Prehn, J. H. M. Patients with mesenchymal tumours and high Fusobacteriales prevalence have worse prognosis in colorectal cancer (CRC). *Gut* **2021**, *71* (8), 1600−1612.
(20) Wong, S. H.; Yu, J. Gut microbiota in colorectal cancer: mechanisms of action and clinical applications. *Nat. Rev. Gastroenterol Hepatol* **2019**, *16* (11), 690−704.
(21) Kong, C.; Yan, X.; Zhu, Y.; Zhu, H.; Luo, Y.; Liu, P.; Ferrandon, S.; Kalady, M. F.; Gao, R.; He, J.; Yin, F.; Qu, X.; Zheng, J.; Gao, Y.; Wei, Q.; Ma, Y.; Liu, J. Y.; Qin, H. Fusobacterium Nucleatum Promotes the Development of Colorectal Cancer by Activating a Cytochrome P450/Epoxyoctadecenoic Acid Axis via TLR4/Keap1/NRF2 Signaling. *Cancer Res.* **2021**, *81* (17), 4485−4498.
(22) Zhang, Y.; Zhang, X.; Yang, H.; Yu, L.; Xu, Y.; Sharma, A.; Yin, P.; Li, X.; Kim, J. S.; Sun, Y. Advanced biotechnology-assisted precise sonodynamic therapy. *Chem. Soc. Rev.* **2021**, *50* (20), 11227−11248.
(23) Son, S.; Kim, J. H.; Wang, X.; Zhang, C.; Yoon, S. A.; Shin, J.; Sharma, A.; Lee, M. H.; Cheng, L.; Wu, J.; Kim, J. S. Multifunctional sonosensitizers in sonodynamic cancer therapy. *Chem. Soc. Rev.* **2020**, *49* (11), 3244−3261.
(24) Canaparo, R.; Foglietta, F.; Barbero, N.; Serpe, L. The promising interplay between sonodynamic therapy and nanomedicine. *Adv. Drug Deliv Rev.* **2022**, *189*, 114495.
(25) Liang, S.; Deng, X.; Ma, P.; Cheng, Z.; Lin, J. Recent Advances in Nanomaterial-Assisted Combinational Sonodynamic Cancer Therapy. *Adv. Mater.* **2020**, *32* (47), e2003214.
(26) Hu, H.; Feng, W.; Qian, X.; Yu, L.; Chen, Y.; Li, Y. Emerging Nanomedicine-Enabled/Enhanced Nanodynamic Therapies beyond Traditional Photodynamics. *Adv. Mater.* **2021**, *33* (12), e2005062.
(27) Tao, N.; Li, H.; Deng, L.; Zhao, S.; Ouyang, J.; Wen, M.; Chen, W.; Zeng, K.; Wei, C.; Liu, Y. N. A Cascade Nanozyme with Amplified Sonodynamic Therapeutic Effects through Comodulation of Hypoxia and Immunosuppression against Cancer. *ACS Nano* **2022**, *16* (1), 485−501.
(28) Li, G.; Wang, S.; Deng, D.; Xiao, Z.; Dong, Z.; Wang, Z.; Lei, Q.; Gao, S.; Huang, G.; Zhang, E.; Zeng, G.; Wen, Z.; Wu, S.; Liu, Z. Fluorinated Chitosan To Enhance Transmucosal Delivery of Sonosensitizer-Conjugated Catalase for Sonodynamic Bladder Cancer Treatment Post-intravesical Instillation. *ACS Nano* **2020**, *14* (2), 1586−1599.
(29) Chen, H.; Zhang, S.; Fang, Q.; He, H.; Ren, J.; Sun, D.; Lai, J.; Ma, A.; Chen, Z.; Liu, L.; Liang, R.; Cai, L. Biomimetic Nanosonosensitizers Combined with Noninvasive Ultrasound Actuation to Reverse Drug Resistance and Sonodynamic-Enhanced Chemotherapy against Orthotopic Glioblastoma. *ACS Nano* **2023**, *17* (1), 421−436.
(30) Rengeng, L.; Qianyu, Z.; Yuehong, L.; Zhongzhong, P.; Libo, L. Sonodynamic therapy, a treatment developing from photodynamic therapy. *Photodiagnosis Photodyn Ther* **2017**, *19*, 159−166.
(31) Li, D.; Yang, Y.; Li, D.; Pan, J.; Chu, C.; Liu, G. Organic Sonosensitizers for Sonodynamic Therapy: From Small Molecules and Nanoparticles toward Clinical Development. *Small* **2021**, *17* (42), e2101976.
(32) Zhu, P.; Chen, Y.; Shi, J. Nanoenzyme-Augmented Cancer Sonodynamic Therapy by Catalytic Tumor Oxygenation. *ACS Nano* **2018**, *12* (4), 3780−3795.
(33) Sun, D.; Pang, X.; Cheng, Y.; Ming, J.; Xiang, S.; Zhang, C.; Lv, P.; Chu, C.; Chen, X.; Liu, G.; Zheng, N. Ultrasound-Switchable Nanozyme Augments Sonodynamic Therapy against Multidrug-Resistant Bacterial Infection. *ACS Nano* **2020**, *14* (2), 2063−2076.
(34) Bai, S.; Yang, N.; Wang, X.; Gong, F.; Dong, Z.; Gong, Y.; Liu, Z.; Cheng, L. Ultrasmall Iron-Doped Titanium Oxide Nanodots for Enhanced Sonodynamic and Chemodynamic Cancer Therapy. *ACS Nano* **2020**, *14* (11), 15119−15130.
(35) Rajora, M. A.; Lou, J. W. H.; Zheng, G. Advancing porphyrin's biomedical utility via supramolecular chemistry. *Chem. Soc. Rev.* **2017**, *46* (21), 6433−6469.
(36) Ma, A.; Chen, H.; Cui, Y.; Luo, Z.; Liang, R.; Wu, Z.; Chen, Z.; Yin, T.; Ni, J.; Zheng, M.; Cai, L. Metalloporphyrin Complex-Based Nanosonosensitizers for Deep-Tissue Tumor Theranostics by Noninvasive Sonodynamic Therapy. *Small* **2019**, *15* (5), e1804028.
(37) Huang, P.; Qian, X.; Chen, Y.; Yu, L.; Lin, H.; Wang, L.; Zhu, Y.; Shi, J. Metalloporphyrin-Encapsulated Biodegradable Nanosystems for Highly Efficient Magnetic Resonance Imaging-Guided Sonodynamic Cancer Therapy. *J. Am. Chem. Soc.* **2017**, *139* (3), 1275−1284.
(38) Shi, J. H.; Sun, S. C. Tumor Necrosis Factor Receptor-Associated Factor Regulation of Nuclear Factor κB and Mitogen-Activated Protein Kinase Pathways. *Front Immunol* **2018**, *9*, 1849.
(39) Zhang, S.; Yang, Y.; Weng, W.; Guo, B.; Cai, G.; Ma, Y.; Cai, S. Fusobacterium nucleatum promotes chemoresistance to 5-fluorouracil by upregulation of BIRC3 expression in colorectal cancer. *J. Exp Clin Cancer Res.* **2019**, *38* (1), 14.
(40) Darding, M.; Meier, P. IAPs: guardians of RIPK1. *Cell Death Differ.* **2012**, *19* (1), 58−66.
(41) Timucin, A. C.; Basaga, H. Pro-apoptotic effects of lipid oxidation products: HNE at the crossroads of NF-κB pathway and anti-apoptotic Bcl-2. *Free Radic Biol. Med.* **2017**, *111*, 209−218.
(42) Li, L.; Wu, W.; Huang, W.; Hu, G.; Yuan, W.; Li, W. NF-κB RNAi decreases the Bax/Bcl-2 ratio and inhibits TNF-α-induced apoptosis in human alveolar epithelial cells. *Inflamm Res.* **2013**, *62* (4), 387−97.
(43) Hoffmann, R.; von Schwarzenberg, K.; López-Antón, N.; Rudy, A.; Wanner, G.; Dirsch, V. M.; Vollmar, A. M. Helenalin bypasses Bcl-2-mediated cell death resistance by inhibiting NF-κB and promoting

https://doi.org/10.1021/acsnano.3c01308
ACS Nano 2023, 17, 11466−11480

reactive oxygen species generation. *Biochem. Pharmacol.* **2011**, *82* (5), 453−63.
(44) Morgan, M. J.; Liu, Z. G. Crosstalk of reactive oxygen species and NF-κB signaling. *Cell Res.* **2011**, *21* (1), 103−15.
(45) Straka, J. G.; Rank, J. M.; Bloomer, J. R. Porphyria and porphyrin metabolism. *Annu. Rev. Med.* **1990**, *41*, 457−69.
(46) Maitra, D.; Bragazzi Cunha, J.; Elenbaas, J. S.; Bonkovsky, H. L.; Shavit, J. A.; Omary, M. B. Porphyrin-Induced Protein Oxidation and Aggregation as a Mechanism of Porphyria-Associated Cell Injury. *Cell Mol. Gastroenterol Hepatol* **2019**, *8* (4), 535−548.
(47) Bellnier, D. A.; Greco, W. R.; Nava, H.; Loewen, G. M.; Oseroff, A. R.; Dougherty, T. J. Mild skin photosensitivity in cancer patients following injection of Photochlor (2-[1-hexyloxyethyl]-2-devinyl pyropheophorbide-a; HPPH) for photodynamic therapy. *Cancer Chemother Pharmacol* **2006**, *57* (1), 40−5.
(48) Dong, Z.; Feng, L.; Hao, Y.; Chen, M.; Gao, M.; Chao, Y.; Zhao, H.; Zhu, W.; Liu, J.; Liang, C.; Zhang, Q.; Liu, Z. Synthesis of Hollow Biomineralized CaCO3-Polydopamine Nanoparticles for Multimodal Imaging-Guided Cancer Photodynamic Therapy with Reduced Skin Photosensitivity. *J. Am. Chem. Soc.* **2018**, *140* (6), 2165−2178.
(49) Feng, L.; Tao, D.; Dong, Z.; Chen, Q.; Chao, Y.; Liu, Z.; Chen, M. Near-infrared light activation of quenched liposomal Ce6 for synergistic cancer phototherapy with effective skin protection. *Biomaterials* **2017**, *127*, 13−24.
(50) Liu, Y.; Liu, C. Z.; Wang, Z. K.; Zhou, W.; Wang, H.; Zhang, Y. C.; Zhang, D. W.; Ma, D.; Li, Z. T. Supramolecular organic frameworks improve the safety of clinically used porphyrin photodynamic agents and maintain their antitumor efficacy. *Biomaterials* **2022**, *284*, 121467.
(51) Yamane, T.; Kanamori, Y.; Sawayama, H.; Yano, H.; Nita, A.; Ohta, Y.; Hinokuma, H.; Maeda, A.; Iwai, A.; Matsumoto, T.; Shimoda, M.; Niimura, M.; Usuki, S.; Yasuda-Yoshihara, N.; Niwa, M.; Baba, Y.; Ishimoto, T.; Komohara, Y.; Sawa, T.; Hirayama, T.; Baba, H.; Moroishi, T., Iron accelerates Fusobacterium nucleatum-induced CCL8 expression in macrophages and is associated with colorectal cancer progression. *JCI Insight* **2022**, *7* (21), DOI: 10.1172/jci.insight.156802.
(52) Shang, F. M.; Liu, H. L. Fusobacterium nucleatum and colorectal cancer: A review. *World J. Gastrointest Oncol* **2018**, *10* (3), 71−81.
(53) Gao, Y.; Bi, D.; Xie, R.; Li, M.; Guo, J.; Liu, H.; Guo, X.; Fang, J.; Ding, T.; Zhu, H.; Cao, Y.; Xing, M.; Zheng, J.; Xu, Q.; Xu, Q.; Wei, Q.; Qin, H. Fusobacterium nucleatum enhances the efficacy of PD-L1 blockade in colorectal cancer. *Signal Transduct Target Ther* **2021**, *6* (1), 398.
(54) Dong, X.; Pan, P.; Zheng, D. W.; Bao, P.; Zeng, X.; Zhang, X. Z. Bioinorganic hybrid bacteriophage for modulation of intestinal microbiota to remodel tumor-immune microenvironment against colorectal cancer. *Sci. Adv.* **2020**, *6* (20), eaba1590.
(55) Xu, C.; Fan, L.; Lin, Y.; Shen, W.; Qi, Y.; Zhang, Y.; Chen, Z.; Wang, L.; Long, Y.; Hou, T.; Si, J.; Chen, S. Fusobacterium nucleatum promotes colorectal cancer metastasis through miR-1322/CCL20 axis and M2 polarization. *Gut Microbes* **2021**, *13* (1), 1980347.
(56) Guo, S.; Chen, J.; Chen, F.; Zeng, Q.; Liu, W. L.; Zhang, G. Exosomes derived from Fusobacterium nucleatum-infected colorectal cancer cells facilitate tumour metastasis by selectively carrying miR-1246/92b-3p/27a-3p and CXCL16. *Gut* **2021**, *70*, 1507.
(57) Chen, S.; Su, T.; Zhang, Y.; Lee, A.; He, J.; Ge, Q.; Wang, L.; Si, J.; Zhuo, W.; Wang, L. Fusobacterium nucleatum promotes colorectal cancer metastasis by modulating KRT7-AS/KRT7. *Gut Microbes* **2020**, *11* (3), 511−525.
(58) Yang, Y.; Jobin, C. Far reach of Fusobacterium nucleatum in cancer metastasis. *Gut* **2020**, DOI: 10.1136/gutjnl-2020-323496.
(59) Chen, Y.; Chen, Y.; Zhang, J.; Cao, P.; Su, W.; Deng, Y.; Zhan, N.; Fu, X.; Huang, Y.; Dong, W. Fusobacterium nucleatum Promotes Metastasis in Colorectal Cancer by Activating Autophagy Signaling via the Upregulation of CARD3 Expression. *Theranostics* **2020**, *10* (1), 323−339.
(60) Stölzel, U.; Doss, M. O.; Schuppan, D. Clinical Guide and Update on Porphyrias. *Gastroenterology* **2019**, *157* (2), 365−381.
(61) Almeida-Marrero, V.; van de Winckel, E.; Anaya-Plaza, E.; Torres, T.; de la Escosura, A. Porphyrinoid biohybrid materials as an emerging toolbox for biomedical light management. *Chem. Soc. Rev.* **2018**, *47* (19), 7369−7400.
(62) Ning, Y.; Jin, G. Q.; Zhang, J. L. Porpholactone Chemistry: An Emerging Approach to Bioinspired Photosensitizers with Tunable Near-Infrared Photophysical Properties. *Acc. Chem. Res.* **2019**, *52* (9), 2620−2633.
(63) Wang, Y.; Yang, H.; Chen, S.; Chen, H.; Chai, Z. Fabrication of Hybrid Polymeric Micelles Containing AuNPs and Metalloporphyrin in the Core. *Polymers (Basel)* **2019**, *11* (3).
(64) Zhang, H.; Liu, H.; Tian, Z.; Lu, D.; Yu, Y.; Cestellos-Blanco, S.; Sakimoto, K. K.; Yang, P. Bacteria photosensitized by intracellular gold nanoclusters for solar fuel production. *Nat. Nanotechnol* **2018**, *13* (10), 900−905.
(65) Kim, Y.; Smith, J. G.; Jain, P. K. Harvesting multiple electron-hole pairs generated through plasmonic excitation of Au nanoparticles. *Nat. Chem.* **2018**, *10* (7), 763−769.
(66) Khaing Oo, M. K.; Yang, Y.; Hu, Y.; Gomez, M.; Du, H.; Wang, H. Gold nanoparticle-enhanced and size-dependent generation of reactive oxygen species from protoporphyrin IX. *ACS Nano* **2012**, *6* (3), 1939−47.
(67) Shangguan, W.; Liu, Q.; Wang, Y.; Sun, N.; Liu, Y.; Zhao, R.; Li, Y.; Wang, C.; Zhao, J. Molecular-level insight into photocatalytic CO(2) reduction with H(2)O over Au nanoparticles by interband transitions. *Nat. Commun.* **2022**, *13* (1), 3894.
(68) Bekalé, L.; Barazzouk, S.; Hotchandani, S. Beneficial role of gold nanoparticles as photoprotector of magnesium tetraphenylporphyrin. *J. Mater. Chem.* **2012**, *22* (7), 2943−2951.